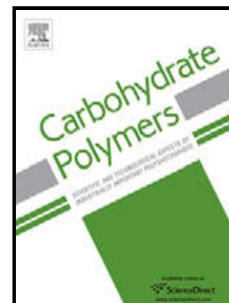


# Journal Pre-proof

Lysine-embedded cellulose-based nanosystem for efficient dual-delivery of chemotherapeutics in combination cancer therapy

Sevil Vaghefi Moghaddam (Investigation) (Methodology) (Project administration) (Writing - original draft), Fatemeh Abedi (Investigation) (Methodology), Effat Alizadeh (Writing - review and editing), Behzad Baradaran, Nasim Annabi (Writing - review and editing), Abolfazl Akbarzadeh (Supervision) (Validation) (Writing - review and editing), Soodabeh Davaran (Validation) (Writing - review and editing)



PII: S0144-8617(20)31034-1

DOI: <https://doi.org/10.1016/j.carbpol.2020.116861>

Reference: CARP 116861

To appear in: *Carbohydrate Polymers*

Received Date: 24 March 2020

Revised Date: 29 July 2020

Accepted Date: 30 July 2020

Please cite this article as: { doi: <https://doi.org/>

This is a PDF file of an article that has undergone enhancements after acceptance, such as the addition of a cover page and metadata, and formatting for readability, but it is not yet the definitive version of record. This version will undergo additional copyediting, typesetting and review before it is published in its final form, but we are providing this version to give early visibility of the article. Please note that, during the production process, errors may be discovered which could affect the content, and all legal disclaimers that apply to the journal pertain.

© 2020 Published by Elsevier.

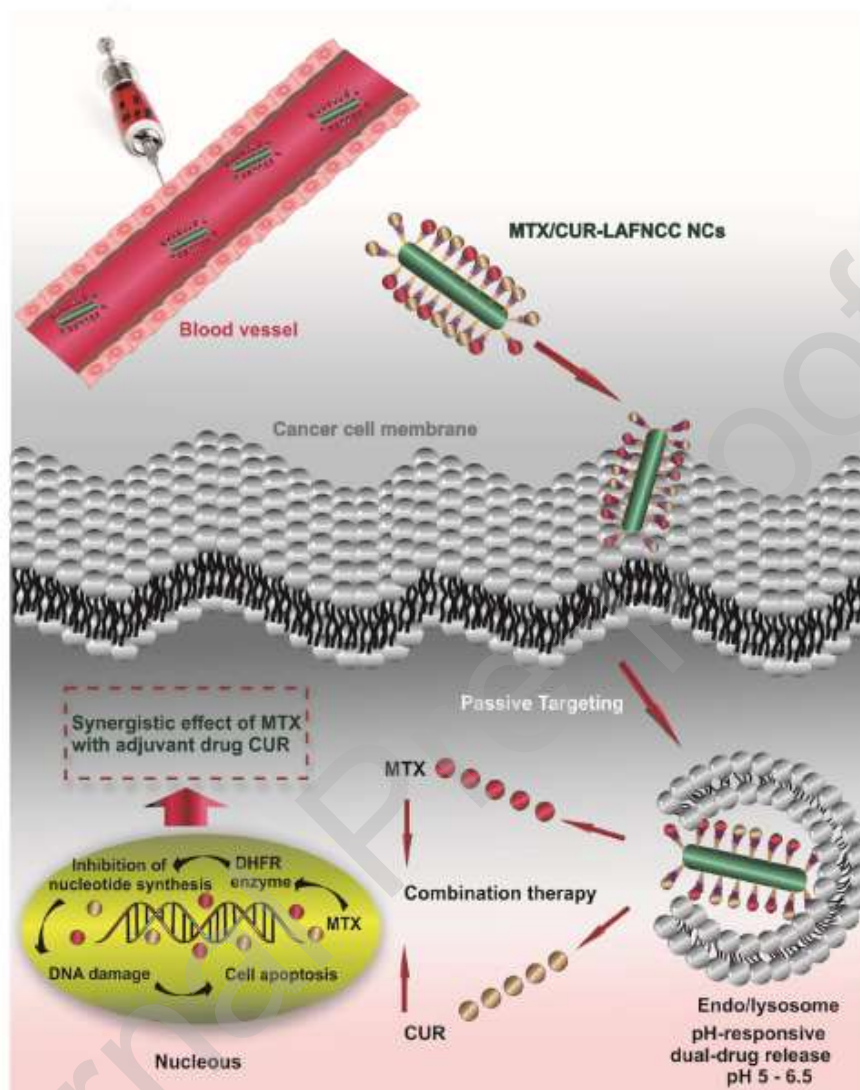
## Lysine-Embedded Cellulose-Based Nanosystem for Efficient Dual-Delivery of Chemotherapeutics in Combination Cancer Therapy

Sevil Vaghefi Moghaddam<sup>1\*</sup>, Fatemeh Abedi<sup>1,2</sup>, Effat Alizadeh<sup>3</sup>, Behzad Baradaran<sup>4</sup>, Nasim Annabi<sup>7\*</sup>, Abolfazl Akbarzadeh<sup>5,6\*</sup>, and Soodabeh Davaran<sup>1,8</sup>

1. Drug Applied Research Center, Tabriz University of Medical Sciences, Tabriz, Iran.
2. Department of Organic Chemistry, Faculty of Pharmaceutical Chemistry, Tehran Medical Sciences, Islamic Azad University, Tehran, Iran.
3. Department of Medical Biotechnology, Faculty of Advanced Medical Sciences, Tabriz University of Medical Sciences, Tabriz, Iran.
4. Immunology Research Center, Tabriz University of Medical Sciences, Tabriz, Iran.
5. Department of Medical Nanotechnology, Faculty of Advanced Medical Sciences, Tabriz University of Medical Sciences, Tabriz, Iran.
6. Universal Scientific Education and Research Network (USERN), Tabriz, Iran.
7. Chemical and Biomolecular Engineering, University of California - Los Angeles, Los Angeles, CA, USA.
8. Department of Medicinal chemistry, Faculty of pharmacy, Tabriz University of Medical Science, Tabriz, Iran.

**Correspondence:** Dr. Sevil Vaghefi Moghaddam, Drug Applied Research Center, Tabriz University of Medical Sciences, Tabriz, Iran. Dr. Abolfazl Akbarzadeh, Department of Medical Nanotechnology, Faculty of Advanced Medical Sciences, Tabriz University of Medical Sciences, Tabriz, Tel: 5154853431. Tel/Fax: +984133341933. Dr. Nasim Annabi, Chemical and Biomolecular Engineering, University of California - Los Angeles, Los Angeles, CA, USA. E-mail: sevil.vaghefi@gmail.com, dr.akbarzadeh2010@gmail.com, annabi.nasim@gmail.com.

Graphical abstract



Schematic illustration for dual-drug delivery of LAFNCC NPs. Once intravenously administrated, the MTX/CUR-LAFNCC NPs accumulated around the tumor site through the enhance permeability and retention (EPR) effect. The MTX/CUR-LAFNCC NPs internalize into the tumor cells by passive tumor targeting mediated-endocytosis and release both MTX and CUR in the acidic pH of the tumor cells. Both drugs delivered to the nucleus to achieve synergistic effect in combination cancer therapy.

## Highlights

- L-lysine decorated modified cellulose nanoparticles are biocompatible.

- MTX/CUR loaded nanoparticles release in sustained and acidic-facilitate manner.
- Adjuvant drug CUR synergize therapeutic efficacy of MTX in MCF-7 and MDA-MB-231.
- Combined drugs represent notable induction of apoptotic cell death than single one.
- Nanocarriers are encouraging delivery platform for combinational cancer therapy.

## Abstract

Combination therapy by two or multiple drugs with different mechanisms of action is a promising strategy in cancer treatment. In this regard, a wide range of chemotherapeutics has used simultaneously to achieve the synergistic effect and overcome the adverse side effects of single-drug therapy. Herein, we developed a biocompatible nanoparticle-based system composed of nanocrystalline cellulose (NCC) and amino acid L-lysine for efficient co-delivery of model chemotherapeutic methotrexate (MTX) and polyphenol compound curcumin (CUR) to the MCF-7 and MDA-MB-231 cells. The drugs could release in a sustained and acidic-facilitate manner. *In vitro* cytotoxicity results represented the superior anti-tumor efficacy of the dual-drug-loaded nanocarriers. Possible inhibition of cell growth and induction of apoptosis in the cells treated with different formulations of CUR and MTX were explored by cell cycle analysis and DAPI staining. Overall, the engineered nanosystem can be used as suitable candidates to achieve efficient multi-drug delivery for combination cancer therapy.

## Keywords

Combination therapy; L-lysine; nanocrystalline cellulose (NCC); dual-drug delivery; sustained release; adjuvant drug; synergistic effect.

## 1. Introduction

Among cancer-related death, breast cancer is the most common leading cause of death in women. In 2018 the American Cancer Society estimated about 266,120 cases for breast cancer, and among them, 40920 (about 14%) women will die from this disease (Bray et al., 2018). Cancer cells present out of control cell proliferation that leads to the formation of lumps and metastasis (Persidis, 1999). One of the most important mechanisms by which cancer cells display resistance to chemotherapeutics is multi-drug resistance (MDR). From the mixed population of malignant cells in tumor lumps, only drug-sensitive cells are destroyed by chemotherapy. In contrast, a large population of drug-resistant cells remain alive and show a partial response to chemotherapy when the tumor regrows (Jain et al., 2014).

As a solution, combination therapy, which deals with co-administration of two or more anti-cancer agents, is a practical alternative over the single-drug treatment (Ahmed et al., 2006; Mi, Zhao, & Feng, 2013; Wang et al., 2011). Generally, combination therapy has shown to promote synergistic anti-cancer response through proper combinations of drugs, which leads to overcoming drug resistance via the variable mechanism of actions that medicines have in the cell growth cycle. Besides, it reduces adverse side effects accompanied by the high dose of single drugs as a result of the development in target selectivity and improved therapeutic efficacy (Al-Lazikani, Banerji, & Workman, 2012; Greco & Vicent, 2009).

Despite the positive features of combinatorial therapy, it still suffers from barriers such as low bioavailability and lack of tumor-specific strategy, resulting in decreased therapeutic efficacy and systemic toxicity, respectively (Peer et al., 2007). Integrating nanocarrier-based systems with combined therapy provides an effective strategy to co-deliver anti-cancer agents to the site of action as well as prevention of blood and renal clearance, leading to the improved bioavailability of drugs in cancerous tissue with minimum toxicity to the adjacent healthy organs (Y. Liu, Fang, Kim, Wong, & Wang, 2014). However, improved efficacy of the co-delivery system with minimal toxicity of drug vehicles is required high drug loading efficiency (Huang, Zhang, Dorn, & Zhang, 2013). Furthermore, since the therapeutic efficacy of drug combinations is directly affected by the release kinetics of individual drugs, the controlled release of drugs is necessary for co-delivery systems (W. Xu et al., 2015).

Most of the previous studies have focused on the design of polymers and nanoparticles (NPs) as carriers in drug delivery systems. As an example, recently, a novel polymer-dendrimer hybrid

NP-based system was designed as a platform for efficient and controlled co-delivery of two anti-cancer agents: doxorubicin (DOX) and paclitaxel (PTX) (Z. Zhao, Lou, Hu, Zhu, & Zhang, 2017). The resulted nanosystem had a unique nano-in-nano structure in which multiple poly(amidoamine) PAMAM dendrimer NPs were embedded in one poly(lactic-co-glycolic acid) (PLGA) NP (Z. Zhao et al., 2017). In another study, to overcome the limitations with single drugs, an amphiphilic molecule with self-assembled property based on docetaxel (DTX) and gemcitabine (GEM) conjugating to the linker poly-ethylene-glycol (PEG) was developed (Kushwah, Katiyar, Agrawal, Gupta, & Jain, 2018). The results showed enhanced therapeutic efficacy and reduced systemic toxicity of developed NPs over conventional free drugs.

A variety of NP-based platforms have been designed to deliver chemotherapeutics to the tumor site including micelles (T. Lu, Sun, Chen, Zhang, & Jing, 2009; H. Xu et al., 2015), dendrimers (Kesharwani & Iyer, 2015; Rahimi, Safa, & Salehi, 2017), liposomes (Bitounis, Fanciullino, Iliadis, & Ciccolini, 2012; ElBayoumi & Torchilin, 2009), and natural and synthetic polymeric nanoparticles (Doppalapudi, Jain, Domb, & Khan, 2016; Tarvirdipour, Vasheghani-Farahani, Soleimani, & Bardania, 2016). Previous studies demonstrated that the use of these NPs as the nanocarrier system could simply solve the problem of low water solubility that is along with the most of the anti-cancer agents, improve their biodistribution, and reduce their toxicity (X. Zhao et al., 2016).

It is noteworthy to pay attention that, most of the nanocarriers discussed in the literature are spherical. In recent years the overwhelming studies on non-spherical nanoplateforms as nanomedicine have been done. There is evidence that elongated nanoparticles have prolonged blood circulation time as well as better extravasation as a result of extensive surface-to-volume ratio, which leads to align in the blood stream and alter the interactions with the phagocytes (Geng et al., 2007). The rod-like nanoparticles prepared from carbon nanotubes (Z. Liu et al., 2007), iron oxide (Park et al., 2009), gold nanorods (J. Choi, Lee, Park, & Kim, 2018), and some other polymers (L. Zhang et al., 2019) represent prolonged blood circulation, and non-cytotoxicity compared with spherical counterparts. An ideal nanocarrier should have the capability to bind reversibly to the hydrophilic as well as hydrophobic drugs. also, it should be responsible for extrinsic stimuli (light, radiofrequency, magnetic field, etc.) or intrinsic stimuli (pH, temperature, redox, etc.). One of the prominent candidates that attracted more attention in

the field of drug delivery could be cellulose NPs or its composition with other polymers (Li et al., 2019). For the cancer therapy, the NPs should be small enough to pass through the biological barriers and accumulates in tumor tissue. Thereby, nanoscale cellulose, known as nanocrystalline cellulose (NCC), is usually used as nanomedicine because of their prominent physicochemical properties such as high aspect ratio due to the rod-like structure, no cytotoxicity, numerous surface hydroxyls that facilitate its surface modification, renewability, and biodegradability (Sunasee et al., 2019). The dimension of the rod-like NCC-based NPs is about 50-1000 nm in length and 1-100 nm in diameters (Habibi, Lucia, & Rojas, 2010; Matos Ruiz, Cavaille, Dufresne, Gerard, & Graillat, 2000). Typically, NCCs are prepared by acid hydrolysis of native and microcrystalline cellulose, leading to the dissolving amorphous regions and imparting negatively charged acidic sulfate esters ( $-\text{OSO}_3^- \text{H}^+$ ) on the surface of crystals via the esterification between surface hydroxyl groups and sulfuric acid molecules. (Azizi Samir, Alloin, & Dufresne, 2005; Habibi et al., 2010; Revol et al., 1994). Therefore, due to electrostatic repulsion between the colloidal particles, the stable aqueous NCC suspension would be obtained (Araki, Wada, Kuga, & Okano, 1998; X. M. Dong, Revol, & Gray, 1998; Rånby, 1951). One of the main disadvantages of NCC NPs is their strong tendency to the irreversible self-agglomeration during the drying process owing to the formation of inter- and intra-molecule hydrogen bonds. The bio-functionalization of NCC is an effective approach to overcome the mentioned problem (Yin, Tian, Jiang, Wang, & Gao, 2016). In this regard, amino acids are suitable candidates since they have not only an important role in the body but also some therapeutic effects in cancer treatment (Marinescu et al., 2006; Tie, Lin, Lee, Bae, & Lee, 2006).

In recent decades, several biomedical applications of amino acid-functionalized polymers, dendrimers, and hyperbranched polymers are reported (Bao, He, & Li, 2012; J. S. Choi et al., 2004; D. Lu, Hossain, Jia, & Monteiro, 2015). Besides, the improvement of cell penetration efficiency by the attachment of positively charged lysine and arginine hyperbranched cores are presented (Aldawsari et al., 2011). L-lysine, known as an essential amino acid, could be generated by the fermentation process that is unstable for long term usage. Therefore, l-lysine hydrochloride is typically employed for application in food, feed additives, and drugs (Fitz, Jakschitz, & Rode, 2008; Zhou, Wu, Chi, & Yang, 2007). Also, it has essential applications in the medical field including production of antibodies, enzymes, and hormones, promoting calcium absorption, and their use for tissue regeneration and repair (Durmus et al., 2009).

Methotrexate (MTX) is one of the typical anti-cancer agents that has commonly used in the treatment of cancers with over-expressing folate receptors on the surface of cancer cells due to the similarity of its structure with folic acid (Barnes et al., 1999). Its therapeutic effect is fulfilled by inhibiting the activity of dihydrofolate reductase (DHFR), an enzyme participating in folate metabolism (Boechat et al., 2015; Roberts, Feeney, Birdsall, Charlton, & Young, 1980; Zeb et al., 2016). However, the cytotoxic effect and poor pharmacokinetics of MTX limited its clinical applications (Cronstein, 2005). Besides, tumor cells may show resistance to the MTX due to either decreasing cellular uptake through diminished folate carriers and receptors or increasing the efflux of MTX (Y.-H. Chen et al., 2007).

Curcumin (CUR), the hydrophobic polyphenolic pigment extracted from turmeric, has a lot of pharmacological effects including antioxidant, anti-inflammatory, wound healing, anti-cancer, and anticoagulant (Aggarwal, Kumar, & Bharti, 2003; Naksuriya, Okonogi, Schiffelers, & Hennink, 2014; Xie et al., 2017). At high concentration, CUR shows anti-cancer and anti-oxidant activity due to the inhibition of tumor cell proliferation through topoisomerase II-mediated DNA cleavage (Y. Zhang et al., 2016). Also, it has proven to overcome the MDR phenomenon through the down-regulation of P-glycoprotein (P-gp) expression (Um et al., 2008). Furthermore, it has a dose-dependent effect on cancer cells (2.5-80 M) while preventing toxicity to healthy cells (Mohan Yallapu, Ray Dobberpuhl, Michele Maher, Jaggi, & Chand Chauhan, 2012; Strimpakos & Sharma, 2008). However, its clinical applications have limited by low stability and water solubility, and inadequate concentration of the drug at tumor site due to the poor uptake and bio-distribution in the body (S. He et al., 2016).

To overcome the problems associated with MTX and CUR utilization in combinatorial therapy, nanomedicine can be used to provide a more efficient strategy for cancer treatment. In this regard, nano formulations of CUR/MTX, along with the sustained release of them from a nanocarriers can increase bioavailability and decrease the required dose of drugs for cancer therapy.

In order to improve nanocarriers efficiency with minimum side effects, stimuli-responsive nanoparticles (NPs), which can produce physicochemical changes in response to external signals (e.g., magnetic field (Tian, Jiang, Chen, Shao, & Yang, 2014), ultrasound (Schroeder et al., 2009), light (Yu et al., 2015)) and internal signals (e.g., pH (Y. Zhang et al., 2016), temperature

(K.-J. Chen et al., 2012), redox potential (Han, Tang, & Yin, 2015), enzymatic activity (Xiong et al., 2012)), were developed. From the various stimuli-responsive NPs, pH-sensitive NPs have attracted special interest as anti-cancer drug delivery systems due to the difference between normal tissue and cancerous tissue (Tang et al., 2011). In pH-responsive nanocarriers, drugs release in the target site based on difference between the pH of the blood and healthy tissue (7.4), the acidic extracellular environment of the tumor (pH 6.0-7.0) and even more acidic environment of intracellular endosomes/lysosomes (pH 5.0-6.5) (S. S. Han et al., 2015).

In the present study, we focused on designing a pH-responsive NP-based system for an efficient and controlled co-delivery of model anti-cancer agents MTX and CUR. The resulting positively charged system is composed of NCC NPs to which amino acid l-lysine was embedded using 3-amino propyl-3-methoxy silane (APTMS) as a bridging molecule. The compound APTMS was used as a coupling agent to react with the surface -OH groups of NCC and produce the more stable etheric linkages. The synthesized nanocarrier was characterized in terms of physicochemical and structural properties. To evaluate the biocompatibility of the designed nanocarrier, the hemolysis assay was carried out. The controlled release of the resulted dual-drug-loaded nanosystem was also examined. Moreover, the *in vitro* cytotoxicity and anti-tumor efficacy evaluation of MTX/CUR-Lys.g.AFNCC NPs were performed by using MCF-7 and MDA-MB-231 human breast cancer cells, as sensitive and resistant cells, respectively. The possible inhibition of cell growth and induction of apoptosis in MCF-7 and MDA-MB-231 cells treated with different formulations of CUR and MTX were also explored by cell cycle analysis and DAPI staining.

## **2. Experimental**

### **2.1. Materials**

Microcrystalline cellulose was purchased from the solarbio company. 3-aminopropyl-3-methoxysilane and MTT (3-(4, 5- dimethylthiazol-2-yl)-2 were acquired from the Acros Organics Company. Fetal bovine serum (FBS, PAA Laboratories), trypsin, penicillin-streptomycin, phosphate buffered saline (PBS), and Roswell Park Memorial Institute 1640 growth medium (RPMI) were ordered from Gibco BRL Life Technologies (Carlsbad, USA). MTX was achieved by Zahravi Pharmaceutical Co. (Tabriz, Iran). Human red blood cells (RBCs) were obtained from the Iranian Blood Transfusion Institute (IBTI). MCF-7 and MDA-

MB-231 human breast cancer cells were purchased from Cell Bank, Pasteur Institute of Iran, Tehran, Iran. All solvents were purchased from Merck Company and used without further purification. Deionized water was used for all experiments and purified with a Milli-Q water system. All other chemicals and reagents were achieved from Sigma-Aldrich Co., Ltd. unless otherwise noted.

## **2.2. Instrumentation**

### **2.2.1. Thermogravimetric analysis (TGA)**

The TGA was conducted using a thermal analysis instrument (SDTA851, Mettler Toledo) in the temperature ranges from 50-800 °C at the heating rate of 10 °C min<sup>-1</sup> under the nitrogen atmosphere. The initial (onset) degradation temperature ( $T_i$ ) along with residual mass percent at 700 °C was defined from the TG curve, while maximum thermal degradation temperature ( $T_{max}$ ) was also collected from DTG peaks maxima.

### **2.2.2. Differential scanning calorimetry (DSC)**

The thermal properties of NCC, AFNCC, and LAFNCC were characterized by DSC using a differential scanning calorimeter (PerkinElmer, Jade). The NCC, AFNCC, and LAFNCC NPs were heated from 25 to 250 °C at the heating rate of 10 °C min<sup>-1</sup> under the nitrogen atmosphere.

### **2.2.3. X-ray Diffraction (XRD)**

XRD analysis of NCC, AFNCC, and LAFNCC NPs was performed using a Bruker D8 ADVANCE diffractometer equipped with a Scintillation control (nal) detector (Bruker AXS, Inc.). The samples were scanned at the speed of 2s per step at step size 0.04° with Cu K $\alpha$  radiation ( $\lambda=1.5406$  Å) over a  $2\theta$  range from 5 to 80° and an anode voltage and current of 40 kV and 35 mA, respectively.

### **2.2.4. Elemental Analysis**

The percentage of carbon (C), hydrogen (H), oxygen (O), and nitrogen (N) content of NCC, AFNCC, and LAFNCC NPs was determined using the elemental analyzer, COStech instruments.

### **2.2.5. Dynamic Light Scattering technique (DLS)**

The particle size distribution and zeta-potential of NCC, AFNCC, and LAFNCC NPs in the aqueous phase was measured at 25 °C using dynamic light scattering (DLS) (Zetasizer Nano ZS90; Malvern Instruments, UK). The concentration of samples was prepared in 0.1 wt%.

#### **2.2.6. Transmission electron microscopy (TEM)**

The TEM images of unmodified NCC, AFNCC, and LAFNCC NPs were taken using Zeiss, Leo 906 microscope 100 kV working voltage. A drop of 0.01 wt% ultrasonically aqueous dispersion of samples was deposited onto the carbon-coated copper grids and allowed to dry at room temperature overnight. The images were processed using ImageJ Software (Schneider, Rasband, & Eliceiri, 2012).

#### **2.2.7. Field Emission Scanning Electronic Microscopy (FESEM)**

The morphological characterization of samples was investigated using field emission scanning electron microscopy (FESEM) (Hitachi, S4160). The samples were settled onto a stub containing carbon and were covered with a conducting layer of gold.

### **2.3. Preparation of nanocrystalline cellulose (NCC)**

NCC suspension was obtained by using a typical acid hydrolysis method with further modification (Zainuddin, Ahmad, Kargarzadeh, & Ramli, 2017). Initially, microcrystalline cellulose (MCC) (5 g) was pre-treated with sulfuric acid 64% in an ice bath under vigorous stirring. Then, the suspension continued to stir constantly at 45 °C for 1 hour. After the completion of the reaction time, the slurry was diluted with cold distilled water to quench the reaction. To remove acid, the suspension was subjected to centrifugation at 9000 RPM for 20 min. The precipitate was dispersed in water and ultrasonically agitated for 10 min. Centrifugation and sonication processes were continued three times. Subsequently, the aqueous suspension was transferred into the dialysis bag (molecular-weight cutoff of 14,000 Da) and dialyzed toward distilled water for several days until the pH of the water reaches to 5.5-6. Finally, nanocrystalline cellulose was received after freeze-drying.

### **2.4. Surface functionalization of NCC with 3-amino propyl-3-methoxy silane (APTMS)**

As the first step, tartaric acid (0.25 mmol, 0.037 g) was added into the toluene/methanol (10:0.5) mixture and stirred thoroughly to dissolve in it. Then, NCC (1 eq, 3.1 mmol, 5g) was added to the solution and dispersed ultrasonically. APTMS (1.5 eq, 4.7 mmol, 0.8 ml) was subsequently added dropwise to the mixture under the nitrogen atmosphere at 80 °C. The reaction mixture was kept under stirring at 80 °C overnight. Amine functionalized nanocrystalline cellulose (AFNCC) NPs were then precipitated by centrifugation (9000 RPM, 20 min). After that, the supernatant was separated, and NPs were dispersed in toluene and centrifuged. This step was repeated twice, followed by washing two times with ethanol (96%) to remove unreacted APTMS. The precipitates were dried inside the vacuum oven overnight and stored in a desiccator for future use.

### **2.5. Preparation of nanocarrier Lys.g.AFNCC (LAFNCC)**

Firstly, the carboxyl group of l-lysine (270 mg) was activated by N, N'-Dicyclohexylcarbodiimide (DCC)/ N-Hydroxysuccinimide (NHS) with the molar ratio of l-lysine: DCC: NHS 1: 1: 1 in 10 mL dimethyl sulfoxide (DMSO) solution at room temperature for 24 h. Then the resultant solution was centrifuged to precipitate the by-product 1, 3-dicyclohexylurea (DCU). The activated l-lysine was remained in the supernatant. Secondly, the activated l-lysine was dripped drop by drop into the 5 ml DMSO solution containing Amine functionalized nanocrystalline cellulose (AFNCC) under the nitrogen atmosphere at room temperature and keep stirring for 24 h. The resultant solution was centrifuged (9000 RPM, 20 min) to precipitate the modified NPs. The precipitate was washed twice with ethanol (96%) to remove unreacted l-lysine. Finally, LAFNCC NPs dried inside the vacuum oven overnight and stored in a desiccator for future use.

### **2.6. *In vitro* hemolysis assay**

The hemolytic activity of LAFNCC was performed according to a previously described procedure with minor modifications (Gao et al., 2016). In brief, an appropriate amount of human fresh blood samples (anticoagulated with ethylenediaminetetraacetic acid (EDTA)), obtained from the Iranian Blood Transfusion Institute (IBTI), diluted with a Phosphate-buffered saline (PBS) and red blood cells (RBCs) isolated from serum by centrifugation at 1500 rpm for 10 min. The precipitated RBCs were washed with PBS several times to remove the total lysis

hemoglobin. Then, the stock suspension was prepared by ten times dilution of the collected RBCs with PBS. The dispersions of LAFNCC NPs were prepared in PBS buffer with the final concentration 5, 10, 20, 40, 80, 160, 320, 640, and 1000  $\mu\text{g}\cdot\text{ml}^{-1}$ . Subsequently, 0.5 ml of the stock suspension was added to 0.5 ml of the NP dispersions and also, 0.5 ml of water and PBS as a positive and negative control with the hemolysis rate of 100% and 0%, respectively. The samples were mixed and incubated for 3 h at 37 °C in an incubator-shaker. Following incubation, the samples were evaluated under an optical microscope using the magnification of 100X. The images were processed by ImageJ Software (Schneider et al., 2012). Finally, the samples were centrifuged (1500 RPM, 10 min), and the supernatants were transferred into the 96-well plate. The samples were assayed for the absorbance of the released hemoglobin at  $\lambda=540$  nm using ELISA-reader. Three independent experiments were conducted for each sample. Hemolysis rate for the different concentration of nanocarrier was determinate by the following equation:

$$\text{Hemolysis rate (\%)} = \frac{A_{(s)} - A_{(-)}}{A_{(+)} - A_{(-)}} \times 100$$

where  $A_{(s)}$ ,  $A_{(-)}$ , and  $A_{(+)}$  are the absorbance of test samples, negative control, and the positive control, respectively.

## 2.7. Preparation of dual-drug loaded LAFNCC nanocarrier

As the first step, 8 mg of MTX was added to 5 ml well-dispersed mixture of nanocarrier in PBS (10 mM, pH 7.4) and continued to stir for 24 h at room temperature in the dark. The resultant product was collected by centrifugation (9000 RPM, 20 min) and the supernatant was taken out to measure the unbounded MTX using its calibration curve that was placed in supporting information (Figure S1). Due to the hydrophobic property of CUR, its dissolution needs to be performed under the sink condition. To increase the water-solubility of the CUR, the surfactant tween 80, and the solvents Methanol (MeOH) and DMSO were added to the dissolution medium (PBS) with the optimum ratio 1: 15.2: 0.8: 83, respectively. For CUR loading, 1 ML of 8 mg/ml solution of CUR in PBS/MeOH/DMSO/Tween 80 was added to re-dispersed MTX loaded NPs in 4 ml of PBS. They mixed thoroughly by sonication for 3 min using 30% amplitude with 30 s ON and 30 s OFF pulses. The mixture gently stirred at room temperature for 24 h in the dark. Finally, MTX/CUR-LAFNCC NPs were collected by centrifugation at 9000 RPM for 20 min, and the supernatant was kept to evaluate the loading content of CUR. The fabricated NPs were

lyophilized and stored at 4 °C for later use. To compare the loading efficiency of drugs in different formulations, the same feeding contents of MTX and CUR were used to prepare MTX-LAFNCC and CUR-LAFNCC. The entrapment efficiency (EE) and loading content (LC) is defined as:

$$EE(\%) = \frac{\text{mass of the loaded drug in NPs}}{\text{mass of total feeding drug}} \times 100$$

$$LC(\%) = \frac{\text{mass of the loaded drug in NPs}}{\text{NPs mass}} \times 100$$

### 2.8. Testing the in-vitro release kinetics of drugs

*In vitro* release kinetics of MTX and CUR from MTX/CUR- LAFNCC nanocarriers (NCs) was evaluated by using a sample and separate method (D'Souza, 2014). In brief, 5 mg of NPs were dispersed in 2ml PBS including 1% (w/w) Tween 80, 15.2 % (v/v) MeOH and 0.8% (v/v) DMSO at two pH values (7.4, 5.0). The release study was conducted under gentle stirring at 37 °C. At predetermined time intervals, 1 mL of released solution (supernatant) was taken out for testing and refilled with equivalent fresh buffer. The amount of MTX and CUR released from MTX/CUR-LAFNCC NCs were detected by UV-visible spectrophotometry at 290 nm and 420 nm, respectively. Each sample in the release study was conducted in triplicate.

### 2.9. *In vitro* cytotoxicity studies

*In vitro* cytotoxicity of free drugs, dual and single drug-loaded nanocarriers was evaluated by MTT assay as reported previously (Curcio et al., 2018). Cells were seeded into 96-well plates at a density of  $15 \times 10^3$  cells/well and incubated for 24 h. Subsequently, the culture medium was replaced with fresh medium, and cells were treated with different concentrations of drug formulations. To verify the biocompatibility of the nanocarrier, cells were treated by blank nanocarrier at different concentrations. Also, untreated cells in the medium were used as a control with 100 % viability. After incubation for 48 h, the culture medium was replaced with fresh medium containing 100  $\mu$ L of MTT (2 mg/mL), and cells were incubated for another 4 h at 37°C. Following incubation, the medium was taken out immediately, and 100  $\mu$ L DMSO was added to solubilize the obtained formazan crystal. Finally, absorbance was measured at 570 nm

using ELISA plate reader (Bio-Tek Instruments, USA). The viability percentage of cells was calculated using the following equation:

$$\text{Cell viability (\%)} = \frac{\text{OD of the treated cells}}{\text{OD of control}} \times 100$$

The inhibitory concentration in half maximum ( $IC_{50}$ ), which is the drug concentration to produce 50% cell death, was calculated using GraphPad Prism 8 (GraphPad Software, Inc., La Jolla, CA). The combination index (CI) values were calculated utilizing CompuSyn v.1 software (T. Chou & Martin, 2005) according to the Chou and Talalay's equation:(T.-C. Chou, 2006)

$$CI_x = \frac{D_1}{(IC_x)_1} + \frac{D_2}{(IC_x)_2}$$

Where,  $(IC_x)_1$  and  $(IC_x)_2$  are the  $IC_x$  of MTX-loaded NPs and CUR-loaded NPs, respectively.  $(D)_1$  and  $(D)_2$  are the concentration of MTX and CUR in the dual drug-loaded NCs at the  $IC_x$  value.

### 2.10. DAPI staining for apoptosis study

To visualize the apoptotic effect of MTX and CUR formulations toward MCF-7 and MDA-MB-231 cells, the nuclei of the cells were stained with DAPI. For this, MCF-7 and MDA-MB-231 cells were seeded onto a 6-well plate at the concentration of  $2 \times 10^5$  cells/well in 2 mL of medium and cultured for 24 h. After incubation for 24 h, the culture medium was replaced with fresh medium containing free drugs, free and drug-loaded nanocarrier in which their concentration was around  $IC_{50}$ , followed by incubation for 48 h. Then, the medium was removed, and the cells were washed with PBS three times. One mL of freshly prepared 4% (w/v) paraformaldehyde was added to each well and incubated for 1h to fix the cells. The fixed cells were permeabilized by adding 0.5 mL of 0.1% (v/v) Triton X-100 and incubated for 5 min. After washing the cells with PBS, the nuclei were stained with  $1 \mu\text{g/mL}$  of DAPI for 10 min incubation. Finally, the cells were imaged using fluorescence microscopy (bio-teck-USA- Citation 5) at  $400\times$  magnification, and excitation at 405 nm for DAPI. The images were processed by using ImageJ Software (Schneider et al., 2012).

### 2.11. Cell Cycle Analysis

To evaluate the therapeutic efficiency of MTX/CUR-LAFNCC NCs, cell cycle analysis was conducted on MCF-7 and MDA-MB-231 cells. For this, cells in the logarithmic growth phase were seeded in a 6-well plate at a density of  $2 \times 10^5$  cells/well and incubated at  $37^\circ\text{C}$  for 24 h. The cells were treated with different formulations of MTX and CUR in which their concentration was around  $\text{IC}_{50}$  as well as blank nanocarrier at a final concentration of  $200 \mu\text{g/ml}$  and incubated for 48 h. The cells were harvested into centrifuge tubes and washed with PBS, then fixed with ethanol 70% and stored at  $4^\circ\text{C}$ . After that, the cells were collected by centrifugation (3000 rpm, 5 min), washed twice with PBS, and resuspended in PBS (300  $\mu\text{l}$ ), followed by the addition of RNase A (10  $\mu\text{g/ml}$ ) and incubation for 30 min. After incubation, DNA intercalating dye PI (10  $\mu\text{g/mL}$ ) was added to the suspension and incubated for 15 min in the dark. The cell distribution in the different cell cycle phases was analyzed from the DNA histogram by Becton-Dickinson FACS Calibur Flow Cytometer and CellQuest software (Becton Dickinson, San Joes, CA, USA).

### 2.12. Statistical analysis

Statistical analysis was conducted using GraphPad Prism 8 (GraphPad Software, Inc., La Jolla, CA). Data were analyzed using one-way ANOVA Analysis of Variance. All the samples were analyzed in triplicates and were presented as mean  $\pm$  standard deviation (SD) for  $n = 3$ . Different combinations of NPs were considered to be statistically significant. The level of significance was calculated by  $p$ -value.  $*P < 0.05$  is considered statistically significant,  $**p < 0.01$ ,  $***p < 0.001$  and  $****p < 0.0001$  are considered highly significant.

## 3. Results and discussion

### 3.1. Preparation and characterization of dual drug-loaded LAFNCC NCs

A biocompatible nanosystem based on cellulose biopolymer was used as a platform to carry anti-cancer drugs including MTX and CUR. As the first step, sulfuric acid hydrolysis of microcrystalline cellulose (MCC) resulted in negatively charged NCC NPs. Subsequently, NPs functionalization was carried out with APTMS, which led to charge reversal of modified NPs. Then, amino acid l-lysine was grafted onto the NPs using amide bond formation between DCC-activated carboxylic acid groups of l-lysine and amine groups of NPs, which in turn increased the amount of positive charge on the surface of NPs. Notably, Grafting of l-lysine onto the surface of NPs prolonged circulation lifetime of NPs in the presence of biological barriers. Finally, MTX

and CUR were loaded to the pH-responsive NPs via electrostatic interactions. The constructional route is illustrated in Figure 1A and 1B.

### 3.2. Characterization

The FT-IR spectra of NCC, AFNCC, LAFNCC, and l-lysine are shown in Figure 1C-F. The peaks at 3300-3500  $\text{cm}^{-1}$  in NCC, AFNCC, and LAFNCC corresponded to the -OH stretching vibration and reflected the tendency of NPs to be hydrophilic. Another relatively broad peak around 2900  $\text{cm}^{-1}$  could be attributed to the aliphatic C-H stretching bond. Additionally, in the spectrum of NCC, the peak around 1640  $\text{cm}^{-1}$  was corresponding to the bending mode of -OH groups of adsorbed water (Hokkanen, Bhatnagar, Repo, Lou, & Sillanpää, 2016). Despite the drying processes, it was difficult to completely remove adsorbed water from NCC due to the cellulose-water interactions. In the NCC spectrum, the peaks at 1432, 1370, 1325, 1114, and 1060  $\text{cm}^{-1}$  were typical nanocellulose absorption peaks that could be assigned respectively as  $\text{CH}_2$  bending,  $\text{CH}_2$  rocking, asymmetrical and symmetrical C-O stretching (Chieng, Lee, Ibrahim, Then, & Loo, 2017). Also, the peak at 1162  $\text{cm}^{-1}$  in the NCC spectrum was corresponding to the sulfate group, owing to the sulfonation of cellulose during the hydrolysis process with sulfuric acid (Chieng et al., 2017). The peak around 1636  $\text{cm}^{-1}$ , which was contributed by N-H bending vibration of primary amine, were observed in the spectrum of AFNCC and LAFNCC, respectively, indicating the successful introduction of the functional groups onto the surface of NCC (Selulosa-Polivinilklorida, SHEL TAMI, KARGARZADEH, & ABDULLAH, 2015). Meanwhile, the N-H stretching was overlapped with the -OH stretching bond. The peaks of Si-O- cellulose and Si-O-Si bridges that referred to the condensation between methoxy groups of silane compound with -OH groups of cellulose, and silanol groups of another silane compound, respectively, were not easily observed by FT-IR since their vibration bands are around 1135 and 1150  $\text{cm}^{-1}$ , which were masked by broad and intense C-O-C vibration band (Britcher, Kehoe, Matisons, & Swincer, 1995). A peak at 1520  $\text{cm}^{-1}$ , which was corresponding to the C=O stretching bond of lysine, is shown in the spectrum of LAFNCC NPs. As a result of overlapping with the N-H bending vibration, the C=O stretching bond was shifted to the lower wavenumbers. The appearance of the carbonyl stretching bond in the spectrum of LAFNCC NPs confirmed the successful embedding of l-lysine onto the surface of amine functionalized NCC.

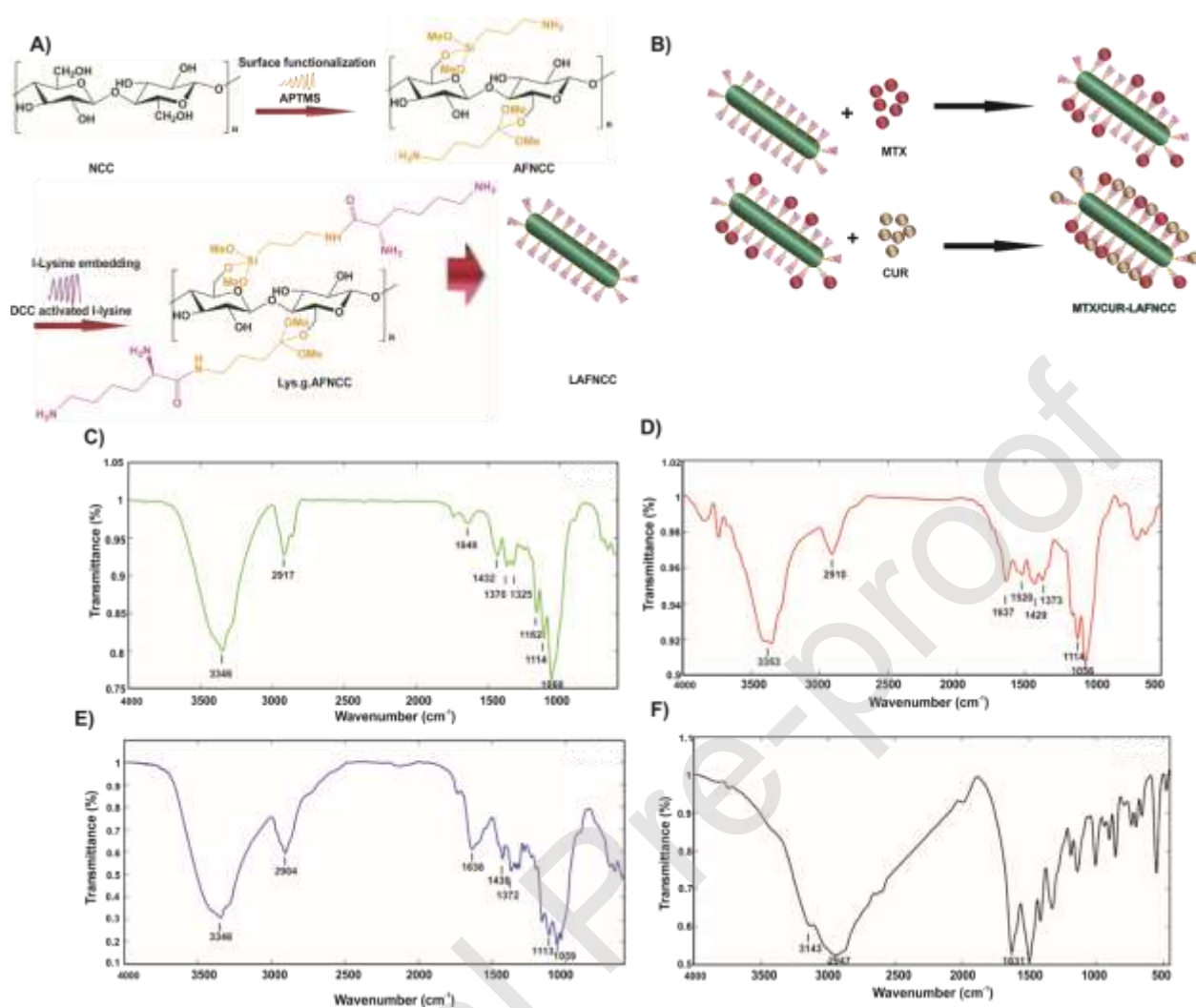
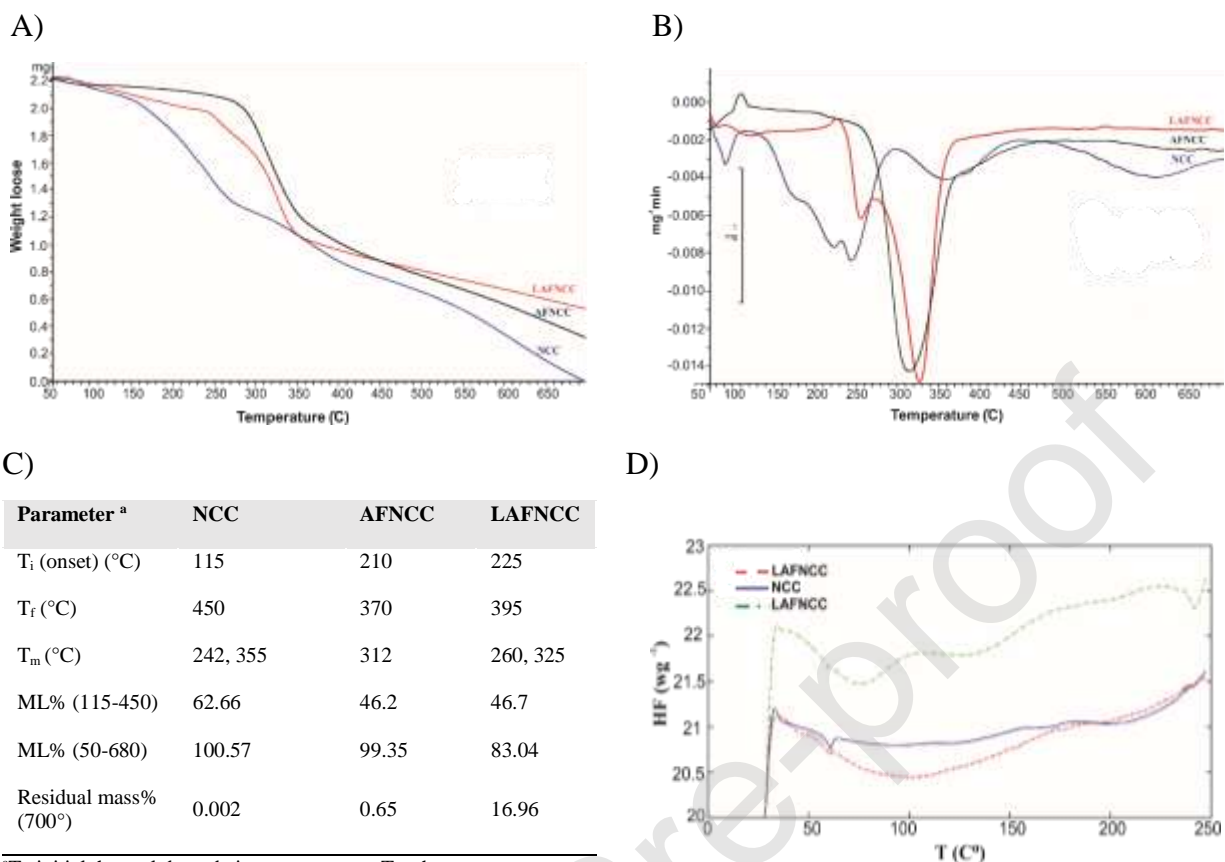


**Figure 1.** Synthetic route and functional groups characterization of MTX/CUR-LAFNCC NCs. A) Synthetic steps of Lys.g.AFNCC NPs fabrication via the formation of etheric bond between NCC and APTMS, followed by the formation of amide bond between L-lysine and AFNCC. B) Schematic representation for the preparation of MTX/CUR-LAFNCC NCs. C-F) FT-IR spectra of NCC NPs, AFNCC NPs, LAFNCC NPs, and L-lysine, respectively.

The thermal stability and degradation profile of NCC, AFNCC, and LAFNCC NPs were assessed by TGA and DTG at 10 °C min<sup>-1</sup> under the N<sub>2</sub> atmosphere (Figure 2). The mass loss and some characteristic temperatures are brought in Figure 2C.



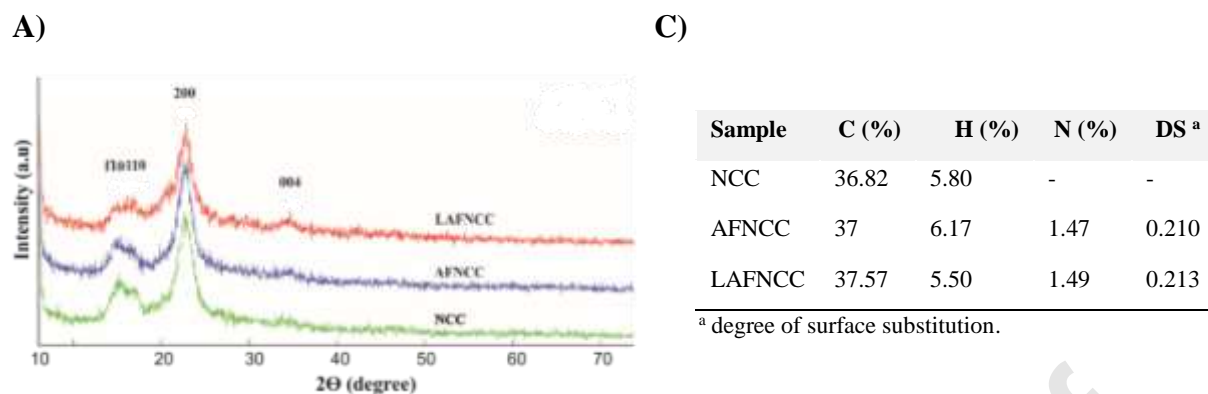
<sup>a</sup>T<sub>i</sub>: initial thermal degradation temperature; T<sub>m</sub>: the temperature at the maximum degradation rate; T<sub>r</sub>: final thermal degradation temperature; ML: mass loss.

**Figure 2.** The thermal properties and degradation profile of NCC, AFNCC, and LAFNCC. A-B) TGA and DTG curves of NCC, AFNCC, and LAFNCC. C) Thermal parameters derived from TGA and DTG data of NCC, AFNCC, and LAFNCC. D) DSC thermograms of NCC, AFNCC, and LAFNCC.

The TGA and DTG curves showed the loss of water around 100 °C (about 3% weight loss) for NCC and AFNCC, indicating that the hydrophilic property of cellulose nanowhiskers was not affected by modification with APTMS (Khanjanzadeh et al., 2017). In contrast, after embedding lysine, the water loss happened at 100-130 °C with 10% weight loss, which referred to improvement in the hydrophilicity of nanowhiskers as a result of increasing the number of interactions with water (Villegas et al., 2017). As shown in Figure 2A and 2B, the main degradation process of NCC had two maximum degradation rates around 242 °C and 355 °C. The lower degradation temperature referred to the highly accessible and more sulfated amorphous regions, while the second peak related to the breakdown of unsulfated crystals

(Dassanayake, Gunathilake, Dassanayake, Abidi, & Jaroniec, 2017). The remained peaks related to the thermal decomposition of cellulose. The DTG curve demonstrated that the modification of NCC with APTMS followed by the embedding of l-lysine onto the surface of NPs increased both initial degradation temperature and temperature with maximum degradation rate, resulting in enhanced thermal stability. The initial degradation temperature ( $T_i$ ) for AFNCC was about 210 °C compared to that of unmodified NCC, which was around 115 °C. After grafting of l-lysine onto the surface of amine functionalized NCC, the initial degradation temperature increased to 225 °C. The main degradation process took place in the range of 115-450 °C, 210-370 °C, and 225-395 °C, corresponding to 62.66%, 46.2%, and 46.7% weight loss for NCC, AFNCC, and LAFNCC, respectively. As depicted in Figure 2B, LAFNCC NPs had a two-step main degradation process. The first one took place in the ranges of 225-270 °C (about 7.6% weight loss), which corresponded to the lysine decomposition. Therefore, the NCC NPs modification could improve dispersion, reduced aggregation, and agglomeration of NPs as well as increased thermal stability. Similar results in terms of improving the thermal stability of nanocellulose after modification reported by some related works (Li et al., 2019; Zainuddin et al., 2017).

DSC was carried out to further confirm the physicochemical characteristics of NCC, AFNCC, and LAFNCC NPs. The  $T_g$  did not profoundly vary among the samples. As depicted in Figure 2D, the glass transition temperature ( $T_g$ ) of NCC, AFNCC, and LAFNCC was found to be 32.86, 34.98, and 33.85 °C, respectively. The difference in  $T_g$  demonstrated some changes in the crystalline and amorphous regions of NCC (Li et al., 2019). The results were in accordance with crystallinity index (Cr.I) in Figure 3B. In all thermograms, endothermic peaks from 50 °C to 170 °C were observed, which were attributed to water evaporation (Ciolacu, Ciolacu, & Popa, 2011). In NCC, maximum temperature of the dehydration process appeared at 65 °C, while AFNCC and LAFNCC had two endothermic peaks with maximum temperature at 65 °C, 100 °C, and 70°C, 130 °C, respectively. The shift of maximum dehydration temperature to the higher values were consistent with the decrease of the crystallinity index (Ciolacu et al., 2011). Another endothermic peak was also observed in the LAFNCC thermogram in the ranges between 235-260 °C. This thermal effect was in accordance with the one observed in TGA/DTG curves, confirming that amino acid l-lysine was successfully grafted onto the surface of cellulose nanocrystals (Martins, Matos, Vicentini, & Isolani, 2005).



**B)**

Sample	Crystallite dimensions <sup>a</sup> (nm)				Interplanar spacings <sup>b</sup> (nm)				CrI <sup>c</sup> (%)
	1 $\bar{1}$ 0	110	200	004	1 $\bar{1}$ 0	110	200	004	
NCC	4.06	3.75	4	3.3	0.583	0.534	0.391	0.259	77.77
AFNCC	4.2	4.9	4.6	4.1	0.586	0.543	0.385	0.258	80.7
LAFNCC	3.8	3.5	3.6	3.2	0.590	0.536	0.390	0.258	76.4

<sup>a</sup> Crystallite dimension in the direction normal to the lattice plans, calculated from  $2\theta$  values using Scherrer equation, using 0.94 for the shape factor. <sup>b</sup> Spacing between the lattice plans, calculated with the Bragg equation. <sup>c</sup> Crystallinity Index.

**Figure 3.** Crystallinity characterization and elemental composition of NCC, AFNCC, and LAFNCC NPs. A) X-ray diffractograms of unmodified NCC, AFNCC, and LAFNCC. B) Crystalline dimensions, Interplanar spacing and Crystallinity Index amounts derived from XRD data of NCC, AFNCC, and LAFNCC. C) Elemental analysis and DS of unmodified NCC, AFNCC, and LAFNCC.

To assess the effect of chemical modification on the crystallinity of cellulose NPs, the powder X-ray diffraction measurements of NCC, AFNCC, and LAFNCC was performed. As shown in Figure 3A, four characteristic peaks were observed at  $2\theta$  angle around  $15.2^\circ$ ,  $16.6^\circ$ ,  $22.7^\circ$ , and  $34.6^\circ$  attributing to the main reflection planes  $1\bar{1}0$ , 110, 200, 004 of the cellulose I lattice, respectively (S. Dong, Cho, Lee, & Roman, 2014). The peaks at  $15.2^\circ$  and  $16.6^\circ$  were related to cellulose I polymorph structure, while the peak at  $22.7^\circ$  corresponded to the crystalline part (Golshan, Salami-Kalajahi, Roghani-Mamaqani, & Mohammadi, 2017).

The relative degree of samples crystallinity was calculated according to the Segal empirical equation (Segal, Creely, Martin Jr, & Conrad, 1959):

$$\text{CrI}(\%) = \frac{I_{200} - I_{\text{am}}}{I_{200}} \times 100$$

where CrI is the crystallinity index of the sample,  $I_{200}$  is the maximum intensity of the cellulose I (the crystallographic plane 200), and  $I_{\text{am}}$  is the diffraction intensity of amorphous cellulose segment at about  $2\theta = 18^\circ$ . According to the results, the crystallinity index of NCC, AFNCC, and LAFNCC were obtained 77.77, 80.7, and 76.4 % respectively indicating that, the crystalline structure of NCC was retained during modification processes and the modification mainly takes place on the surface of NPs.

The crystallite dimensions, interplanar spacing, and CrI for NCC, AFNCC, and LAFNCC are listed in Figure 3B. The interplanar spacings of the AFNCC and LAFNCC were nearly the same as those of the cellulose NPs (NCC), demonstrating that chemical modification had no impact on crystal lattice of particles. However, it caused a slight change in crystallite dimensions and degree of crystallinity. Meanwhile, modification with APTMS caused an increase in dimensions normal to  $1\bar{1}0$ , 110, 200, and 004 lattice planes. In contrast, the embedding of l-lysine onto the surface of NPs decreased dimensions normal to  $1\bar{1}0$ , 110, 200, and 004 lattice planes. This could be evidenced by the recorded crystallinity index in Figure 3B. It should be noted, however, that the crystallite dimensions did not necessarily indicate the dimensions of the NPs.

The elemental composition of NCC, AFNCC, and LAFNCC was evaluated by elemental analyses. The results listed in Figure 3C revealed that in contrast to unmodified NCC, the NCC modified with APTMS followed by l-lysine contained atomic nitrogen confirming the successful modification of cellulose NPs. The percent of atomic nitrogen, however, was slightly more in LAFNCC in comparison to AFNCC and attributed to both APTMS and l-lysine.

The degree of surface substitution (DS) determined by the nitrogen percentage evaluated by elemental analysis based on the equation reported in the related studies (Song, Zhang, Gan, Zhou, & Zhang, 2011; Zainuddin et al., 2017).

$$\text{DS} = \frac{162 \times \text{N} \%}{14 - 179.29 \times \text{N} \%}$$

Where the values of 14, 162, and 179.29 represent the molar mass of nitrogen, Anhydrous glucose unit (AGU), and APTMS, respectively. The results in the Figure 3C indicate that NPs were modified with a small degree of substitution, even these low degrees of substitution made them a proper candidate for drug loading based on electrostatic interactions.

To determine the particle size distribution and surface charge of prepared nanocarrier by dynamic light scattering (DLS) and zeta potential technique, the dried NPs re-dispersed ultrasonically using prob type sonicator (300 w, 20 s). As shown in Figure 4E, at pH 7.4, the average size of unmodified NCC, AFNCC, and LAFNCC was determined 336.7, 514, and 537 nm respectively, suggesting the successful modification of NCC NPs. However, there was a small difference in the average hydrodynamic particle size of NPs at pH 5.0 in comparison to pH 7.4. The resultant particle size was different from the particle size diameter measured for dry sample by SEM and TEM, since in DLS the hydrated diameter of particles in the liquid is determined. Meanwhile, the zeta-potential values for all of the samples are shown in Figure 4D. The unmodified NCC possessed negative zeta-potential due to the presence of sulfate ester ( $\text{OSO}_3^-$ ) groups arising from sulfuric acid in the hydrolysis process. The present observation showed that the zeta potential for NCC dispersion varied between -33.1 at pH 7.4 to 0.0 at pH 5.0, which is in accordance with the earlier report (Molnes, Paso, Strand, & Syverud, 2017). In contrast, AFNCC and LAFNCC had positive zeta-potential as a result of amine groups protonation at pH 7.4, which further confirmed the successful amine surface modification. Increasing the number of amine groups in LAFNCC causes a more positive charge in comparison to AFNCC. Also, the slight decrease in the zeta potential of the prepared LAFNCC nanocarrier at pH 5.0 is probably due to the deprotonation of silanol groups (Si-OH) of the surface. All the results implying to the pH-responsive property of the LAFNCC nanocarrier. The size distribution and morphology of the NPs were assessed by TEM. As shown in Figure 4A, the re-dispersed LAFNCC NPs were rod-like with lower transparency and the length of about  $240.68 \pm 124.58$  nm. The high transparency of the nanoparticles represent their weak contrast with the carbon coating of the copper grids, suggesting their thin nature (Xing, Chen, Liang, et al., 2018). Potentially, the wide range of NPs length was due to the poorly separation of multiple individual whiskers during the production. No apparent structural change was observed after the functionalization of NCC with APTMS and modification with L-lysine.

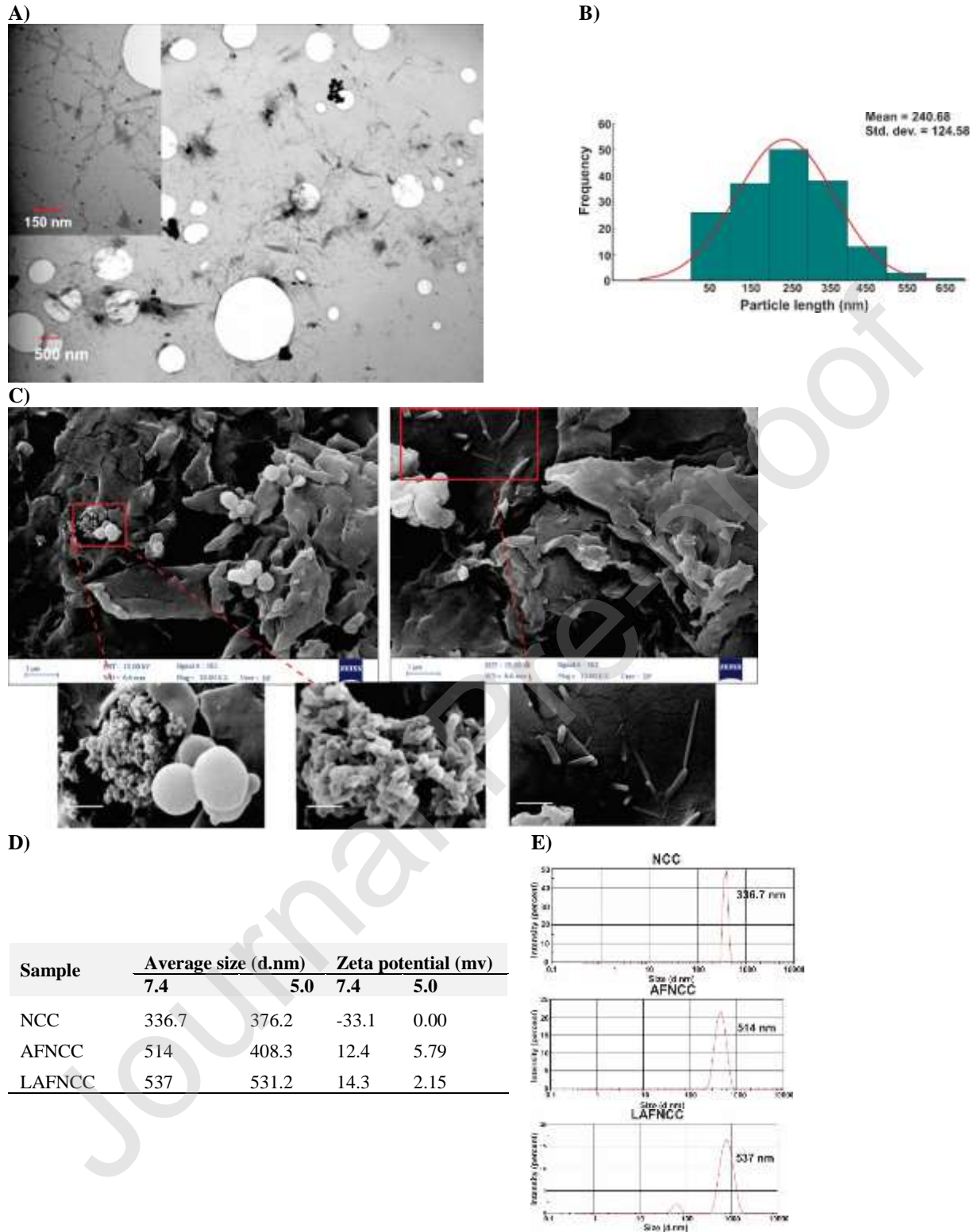


**Figure 4.** Characterization of the morphological and physicochemical properties of the NPs. A) TEM images representing the structure of the LAFNCC NPs. B) Particle size distribution of

LAFNCC NPs. C) FESEM micrographs of LAFNCC fabricated from the freeze-dried NCC NPs. Scale bars represent 1  $\mu\text{m}$  and 200 nm. D) Physicochemical properties of NCC, AFNCC, and LAFNCC NPs at two pH values 7.4 and 5.0. E) The hydrodynamic size distribution of NCC, AFNCC, and LAFNCC NPs at pH 7.4.

The SEM micrograph of freeze-dried LAFNCC NPs are represented in the Figure 4C. It is evident that after freeze-drying, NCC NPs agglomerated as a result of increasing the number of hydrogen bonds. So, the structure of the freeze-dried NCC NPs changed mostly from rod-like to flaky-like (Beck, Bouchard, & Berry, 2012). However, as can be seen in the bottom of the image (right), due to the total removal of the amorphous part in some regions of the NPs, the individual rod-like structure with smooth surface was observed or disintegration of nanorods in some parts take place during the hydrolysis process (Khili, Borges, Almeida, Boukherroub, & Omrani, 2019). The modification did not alter the morphology of NPs significantly. After functionalization with the APTMS, the silyl groups were found in the spherical form.

### 3.3. Hemocompatibility assay

The evaluation of hemocompatibility is a critical issue in the design of nanocarriers as a result of the intravenous injection administration of the drug carriers in drug delivery systems. Hemolysis is the most typically used technique to assess the effect of injected material on the blood, since, in this way, the results of the *in vitro* study are in agreement with the results of *in vivo* study. Erythrocytes or red blood cells (RBCs), which are the most common in the blood, are responsible for delivering oxygen to the tissues and removal of carbon dioxide from them as well as taking part in acid-base blood balance. Therefore, in hemolysis, the ability of nanocarriers to damage erythrocytes is the commonly applied method of their toxicity assessment. As a result of erythrocyte destruction, hemoglobin releases from the erythrocyte plasma membrane to the blood, which is the sign of blood poisoning by any foreign material. It is noteworthy that, transition in physicochemical features of erythrocytes like size, surface charge, and shape determine their interactions with nanocarriers.

Here, the effect of the fabricated nanocarrier LAFNCC on the shape and morphology of the RBCs have investigated by an optical microscope. In this regard, they were treated with various concentrations of nanocarrier (5-1000  $\mu\text{g ml}^{-1}$ ) as well as PBS buffer (pH 7.4), and deionized

water as the negative and positive control, respectively. After incubation for 3 h, the shape changes of RBCs were investigated through the optical microscope (Figure 5B). Treated of RBCs with PBS buffer did not alter the normal discocyte form while treated with deionized water, induced complete hemolysis of erythrocytes. The images in the Figure 5B imply that RBCs treatment with  $1000 \mu\text{g ml}^{-1}$  nanocarrier, cause partly echinocytes formation due to the interactions of nanocarrier with the membrane of RBCs. As shown in Figure 5A, the hemolysis rate was used to analyze the biocompatibility of the LAFNCC NPs in different concentrations. It was observed that LAFNCC NPs had a negligible hemolytic effect in a concentration-dependent manner, which was lower than the acceptable doses so that it could make it suitable for the *in vivo* application. Therefore, the fabricated LAFNCC NPs up to  $1000 \mu\text{g mL}^{-1}$  were found ideal for intravenous injection application.

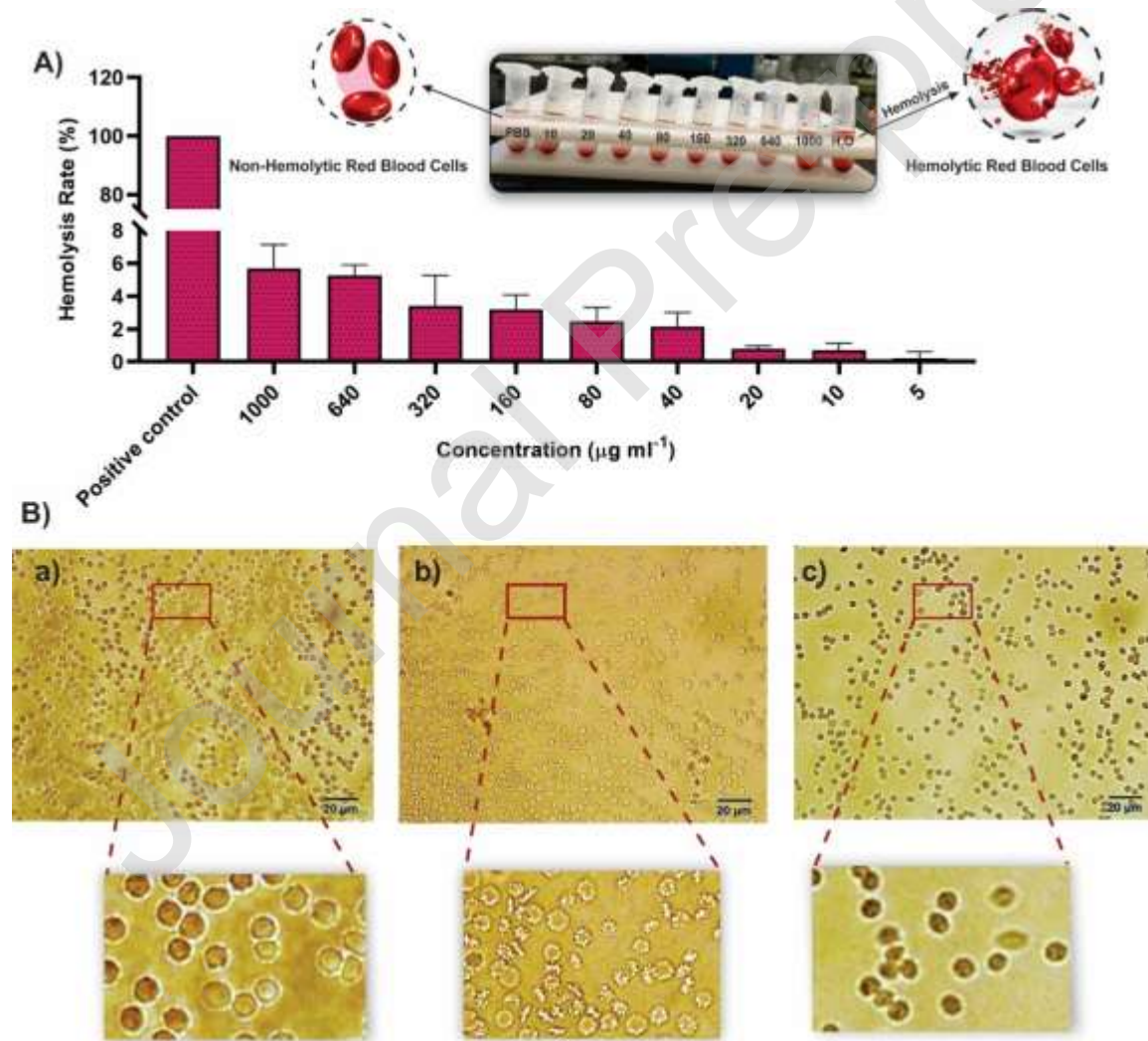


**Figure 5.** A) Hemolysis rate of RBCs being exposed to different concentrations of LAFNCC NPs to estimate their potential effects on the lysis of RBCs followed by releases of hemoglobin to the supernatant. Data are the mean  $\pm$  standard deviation of three independent experiments. PBS and water were used as a negative and positive control, respectively. B) the optical images of RBCs using magnification  $\times 100$ . The images include the RBCs in the presence of a) PBS, b) water and, b) 1000  $\mu\text{g/ml}$  of LAFNCC NPs.

### 3.4. Fabrication of MTX/CUR- loaded LAFNCC and their *in vitro* release study

MTX and CUR were used as model drugs to examine the loading and release profile of the pH-responsive LAFNCC NPs. One of the main advantages in the fabrication process of MTX/CUR-LAFNCC NPs is the simplicity of the co-loading method via the dispersion of the nanoparticles in the solution of MTX and CUR, respectively. It is the most common method for drug loading in the nanocarriers, so that Xing et. al. also used the same method for DOX loading into the cellulose/MXene hydrogels by immersion of hydrogels in the solution of DOX (Xing, Chen, Liang, et al., 2018). The embedding of MTX and CUR on the surface of NPs was mostly via the surface adsorption and hydrophobic interactions. The amine groups of NPs ( $\text{pKa}$  9.5-10) and carboxylic acid groups of MTX ( $\text{pKa}_1$  4.7,  $\text{pKa}_2$  5.6), change into the ( $\text{NH}_3^+$ ) and ( $\text{COO}^-$ ) at pH 7.4, which led to the formation of the hydrogen bond between the moieties mentioned above (Rahimi, Shafiei-Irannejad, Safa, & Salehi, 2018; Singh & Subudhi, 2016). Moreover, the hydrophobic interactions of CUR with the NPs along with the hydrogen bond formation between enolate groups of the CUR ( $\text{pKa}_1$  7.4) and protonated amine groups of the NPs provide CUR surface absorption (Martínez-Guerra et al., 2019). To achieve the synergistic effect induced by administered drugs, feeding drug ratio, 1:1 was selected for MTX/CUR- LAFNCC NCs. The entrapment efficiency for MTX and CUR was found to be 33% and 75% respectively, which was calculated based on unbounded drug concentration, and the loading content was 3.3% and 7.5%, respectively, as a result of feeding ratio 10:1 of nanocarrier to each of the administered drugs.

To validate the effect of intrinsic stimuli pH on the release profile of MTX and CUR from the nanocarriers the *in vitro* release study was investigated at both physiological pH (pH 7.4) and lysosomal pH (pH 5.4) at 37 °C. Some of the important biological protocols that should be taking into account in designing nanomedicines with probable clinical applications including blood circulation, tumor penetration, vessel extravasation as well as efficient tumor cell uptakes

before the drugs are released. Although the smaller nanoparticles are preferred for deep tumor penetrations, they are quickly cleared during blood circulation, leading to insufficient drug accumulation in the tumor site. To overcome these obstacles, size shrinkable or intelligent nanoplatforms have been designed. However, compared with them whose design is complicated, the co-loaded nanoplatform MTX/CUR-LAFNCC could be a promising alternative for conquering the penetration problem. The acidic tumor microenvironment favors the release of drugs from the nanoplatform, and in this way, the released small drug molecule will be well fitted to high tumor penetration. In this regard, Tao et al. have also designed a novel antimony-based nanosheets, namely AM-PEG/DOX NSs, whose release in tumor site was based on pH (intrinsic stimuli) and NIR (near infra-red) irradiation (extrinsic stimuli) (Tao et al., 2018). As depicted in Figure 6B and 6D, the releases of MTX and CUR from dual drug-loaded LAFNCC NCs were more efficient at pH 5.4 than at pH 7.4. At lower pH value, the protonation of methotrexate carboxylate groups ( $pK_{a2}$  5.6) along with the reduction in surface charge, eliminates electrostatic interactions with the ammonium groups of the nanocarrier, leading to the quickening in MTX release (Figure 6A and 6B). Also, protonation of the enolate group in curcumin ( $pK_{a1}$  7.4) promotes the release of CUR from the nanocarrier. Interestingly, due to the strong hydrophobic interactions of curcumin with the nanocarrier, lower release percentage, as well as sustain release pattern was obtained in comparison to MTX at both pH 7.4 and 5.4 (Figure 6C and 6D). At pH 7.4, after 96 h, the cumulative release percentages for MTX and CUR in dual-drug-loaded nanocarrier are 52.44% and 47.94%, respectively. In contrast, at pH 5.4 the cumulative release percentages of drugs are 56.51% and 53.95%, respectively in this interval. As the release of MTX and CUR was controlled by disruption of electrostatic interactions, the pH-responsive release of MTX and CUR was evident. The negligible release of MTX and CUR from the nanocarrier at pH 7.4 could reduce unwanted side effects in healthy tissue while circulating in the body. Once the nanocarriers reached the tumor site and internalized the cancer cells, the acidic microenvironment of the cells stimulates the destruction of electrostatic interactions via protonation of the drugs. As a result, MTX and CUR would come out in a controlled manner inside the cancer cells, which led to an increase in the bioavailability to the tumor site.

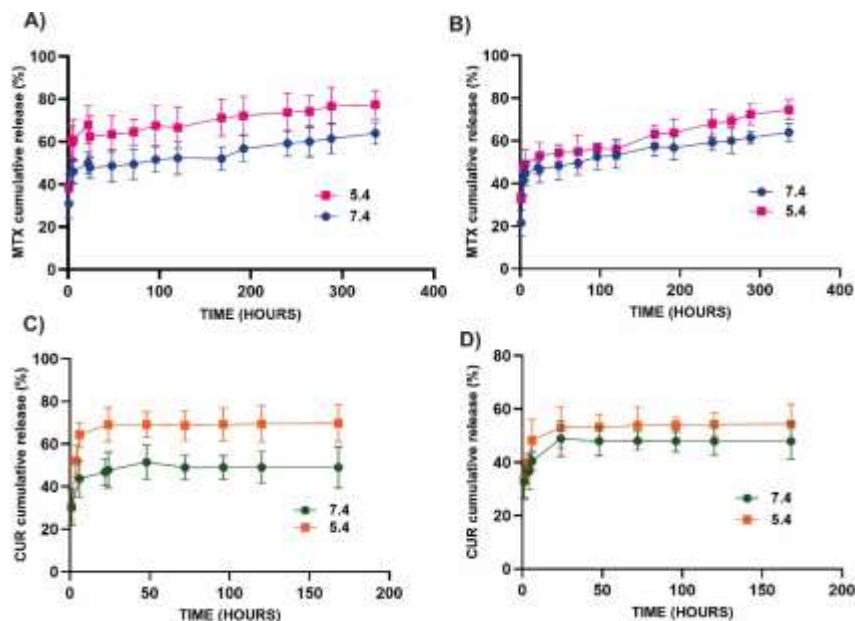


**Figure 6.** *In vitro* release kinetics of loaded drug formulations. A) The release profile of MTX from MTX-LAFNCC NCs at pH 7.4 and 5.4. B) The release profile of MTX from MTX/CUR-LAFNCC NCs at pH 7.4 and 5.4. C) The release profile of CUR from CUR-LAFNCC NCs at pH 7.4 and 5.4. D) The release profile of CUR from MTX/CUR-LAFNCC NCs at pH 7.4 and 5.4.

### 3.5. *In vitro* cytotoxicity studies against breast cancer cells

The anti-tumor efficacy of MTX and CUR in different formulations was evaluated using MTT assay for 48 h, in MCF-7 and MDA-MB-231 breast cancer cells. MCF-7, known as mildly malignant human breast cancer epithelial cell, while MDA-MB-231 is defined as malignant human breast cancer epithelial cell. Both of them derived from the mammary gland of breast tissue. MCF-7 and MDA-MB-231 are classified into luminal A and basal-like immunohistochemistry (IHC) subtypes, respectively (Abramczyk et al., 2015). The viability of the cells treated with different concentration of drug formulations was shown in Figures 7B and 7C. As depicted in Figure 7A, no obvious evidence of cytotoxicity was observed for both cancer cells after treated with different concentrations of non-drug-loaded LAFNCC NPs, representing excellent cytocompatibility of the NPs while using as a carrier. On the other words, the blank LAFNCC NPs exhibit does-dependent reduction in cell viability so that, as depicted in figure 7A, by increasing the nanoparticles concentration, the slop of the graph decreased mildly in both cells. The same results were reported by Xing et al. in which the neat cellulose hydrogel was

assessed nontoxic toward both normal and cancer cells including, B16 (mouse melanoma), SMMC-7721 (human hepatocellular carcinoma), and J774A.1 (mouse macrophage) cells (Xing, Chen, Qiu, et al., 2018). Besides, decorating of nanocarriers with amino acid L-lysine further enhance the biocompatibility of the resultant nanoparticles (Wu et al., 2020).

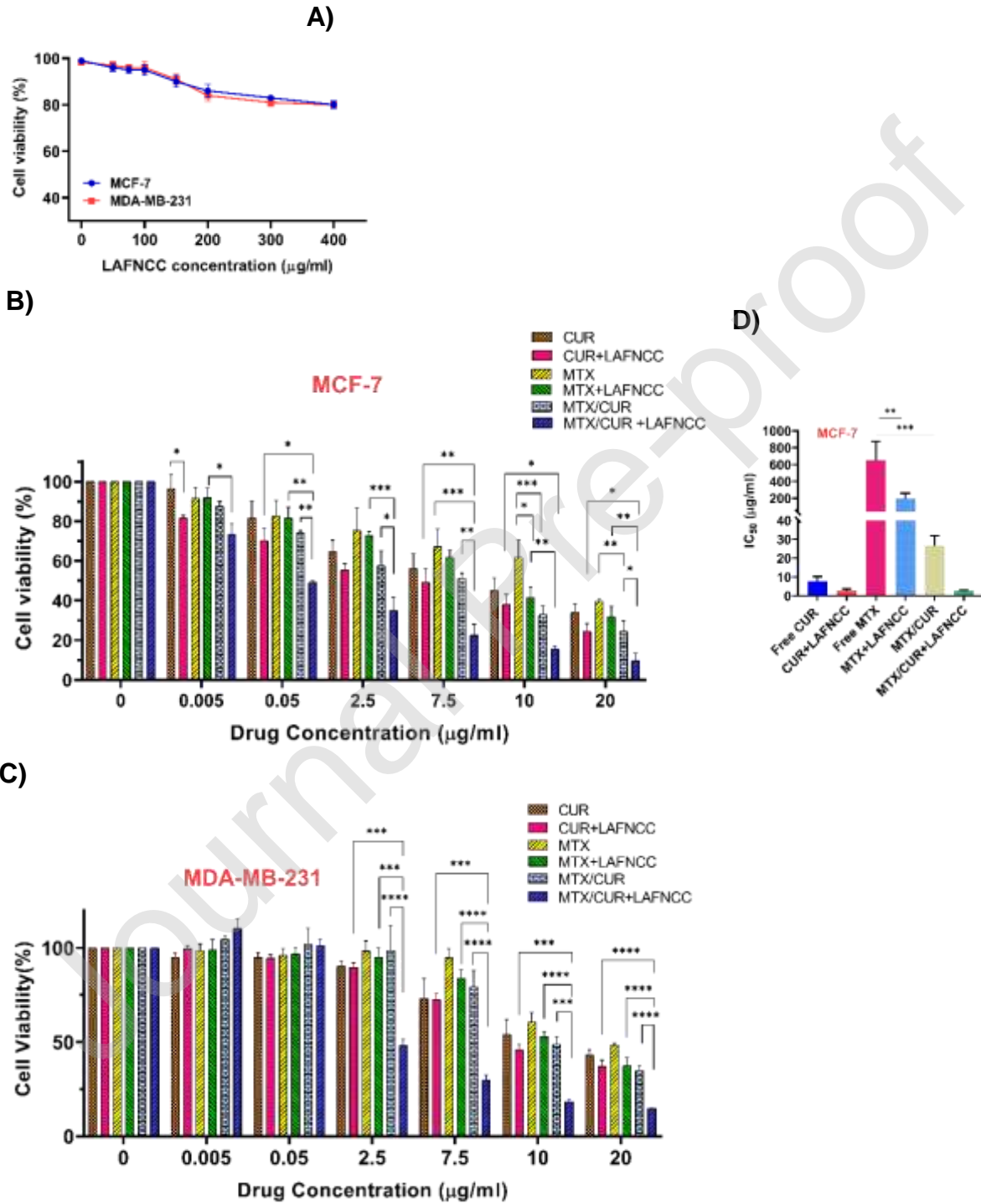


**Figure 7.** *In vitro* cytotoxicity of MTX and CUR formulations in MCF-7 and MDA-MB-231 cells. A) Cell viability of MCF-7 and MDA-MB-231 cells after treatment with different concentrations of non-drug-loaded LAFNCC NPs. B-C) Cell viability of MCF-7 and MDA-MB-231 cells after being exposed to various doses of MTX and CUR formulations. D-E) The  $IC_{50}$  comparison of the different drug formulations in MCF-7 and MDA-MB-231 cells. MTX/CUR ratio in free MTX/CUR and MTX/CUR-AFNCC NCs was all around 1:1. Comparison among groups was conducted by one-way ANOVA followed by Tukey's HSD analysis, \*  $p < 0.05$ , \*\*  $p < 0.01$ , \*\*\*  $p < 0.001$ , \*\*\*\*  $p < 0.0001$ .

Along with the previous reports, in both cell lines, MTX and CUR represented a dose-dependent effect in all of the formulations. Combination treatment of the drugs resulted in more significant loss in the cell viability, especially in higher doses, in comparison with the single-drug formulations, suggesting synergistic growth inhibitory effect of MTX and CUR on MCF-7 and MDA-MB-231 cells. To verify the synergistic effect of dual-drug-loaded LAFNCC NPs, half-maximum inhibition concentration ( $IC_{50}$ ) of MTX and CUR in various formulations along with combination index ( $CI_x$ ) of MTX/CUR-LAFNCC NCs with mass ratio 1:1 of MTX/CUR, and their cytotoxicity has compared. The amount of combination index is a critical indicator to evaluate the pharmacological interactions between two or more drugs, and a value  $< 1$ ,  $= 1$ , and  $> 1$  demonstrate to the synergistic, additive, and antagonistic effects, respectively. Figure 8A represents the dose-effect parameters including  $m$ ,  $D_m$ , and  $r$  that indicate the slope of the median-effect plot (shape parameter), the dose of median-effect (potency parameter like  $IC_{50}$ ), and linear correlation coefficient of the median-effect plot (conformity parameter), respectively (T.-C. Chou, 2006).

The  $CI$  values at actual experimental points along with different effect levels ( $F_a$ ) and type of interaction for MCF-7 and MDA-MB-231 were presented in Figure 8C, respectively. The  $CI$  values ranged from 4.004 to 0.003 for MCF-7 and 12.627 to 0.075 for MDA-MB-231, indicating antagonistic effect ( $CI > 1$ ), medium synergistic effect ( $0.7 < CI < 1$ ), synergistic effect ( $0.3 < CI < 0.7$ ), strong synergistic effect ( $CI < 0.3$ ). A graphical representation of the obtained results was combination index curves ( $F_a$ - $CI$  plot), in which the  $CI$  values were plotted against the corresponding effect levels (Figure 8B).

A)

Cell line	drug	m	D <sub>m</sub>	r
MCF-7	MTX	0.48	186.00	0.9830
	CUR	0.26	1.77	0.9450
	MTX+CUR	0.57	2.35	0.9522
MDA-MB-231	MTX	0.82	507.25	0.9875
	CUR	0.61	17.44	0.9506
	MTX+CUR	1.19	13.65	0.9591

The data were collected from MTT assays and were subjected to the automated calculation of m, D<sub>m</sub>(μg/ml), and r parameters using CompuSyn software.

C)

Drug concentration (μg/ml)			MCF-7			MDA-MB-231		
MTX	CUR	MTX+CUR	CI	F <sub>a</sub>	Interaction type	CI	F <sub>a</sub>	Interaction type
2.5	0.005	0.3	4.004	0.266	Antagonism	4.474	0.021	Antagonism
5	0.05	3	0.757	0.508	Medium synergism	12.627	0.044	Antagonism
23	2.5	16	0.449	0.649	Synergism	0.396	0.528	Synergism
47	7.5	30	0.085	0.774	Strong synergism	0.218	0.706	Strong synergism
470	10	37	0.020	0.843	Strong synergism	0.097	0.820	Strong synergism
940	20	43	0.003	0.902	Strong synergism	0.075	0.854	Strong synergism

B)

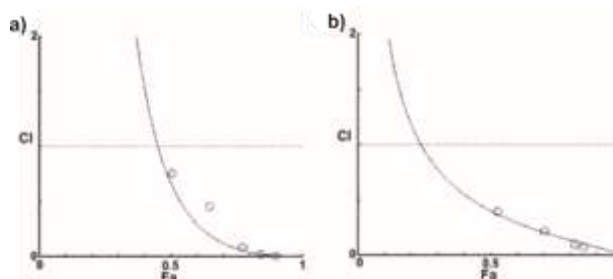


**Figure 8.** A) Dose-effect parameters for MTX and CUR in MCF-7 and MDA-MB-231 cells. B) The combination index plot (Fa-CI plot) for MTX and CUR co-treatment on a) MCF-7, b) MBA-MB-231 cells. CI values are plotted as a function of the Fractional inhibition (Fa) of cell viability/ growth by computer simulation (CompuSyn software). C) The combination index values for MTX and CUR in the MCF-7 and MDA-MB-231 cells.

Furthermore, through the analysis of the CIs for a wide range of effect levels, the half-maximum combination index values for dual-drug-loaded LAFNCC NPs in MCF-7 and MDA-MB-231 cells were calculated 0.66 and 0.41, respectively indicating the moderate synergistic effect of MTX and CUR. Next, the cytotoxic effect of free drugs and single-drug-loaded nanocarrier was compared. As shown in Figure 7B and 7C, in both cancer cells, single-drug-loaded nanocarrier has remarkably enhanced anti-tumor efficiency in comparison to free drugs ( $p < 0.05$ ). This effect can be related to the ability of nanocarrier to increase drug entrance inside the cells using the endocytic process. The amount of IC<sub>50</sub> for different drug formulations in MCF-7 and MDA-MB-231 cancer cells demonstrated in Figure 7D and 7E. More interestingly, the enhanced

cytotoxicity of MTX/CUR-loaded nanocarrier in comparison to MTX-loaded nanocarrier in both cancer cells suggested the adjuvant performance of CUR in decreasing the proper dosage of chemotherapeutic MTX as well as severe systemic toxicity comes by that drug (Bessone et al., 2019). CUR considerably synergized the therapeutic effect of MTX in both MCF-7 and MDA-MB-231 cells through the induction of apoptotic cell death. The amount of  $IC_{50}$  for MTX-loaded nanocarrier was 120.8 and 483.8 for MCF-7 and MDA-MB-231 cells, respectively. However, when the cells treated with CUR along with MTX in MTX/CUR-LAFNCC formulation, it decreased to 2.258 for MCF-7 and 15.84 for MDA-MB-231. The observed results indicate that CUR has synergistic property beside MTX. The synergistic effect of MTX and CUR combination arises from the activation of different signaling pathways. MTX competitively inhibits the enzyme dihydrofolate reductase (DHFR), which converts dihydrofolate (DHF) to tetrahydrofolate (THF). The tendency of MTX to the DHFR is more than folate. Folic acid is necessary for de novo synthesis of purine and pyrimidine, which are required for DNA synthesis. As a result, MTX by inhibition of DNA, RNA, and protein formation causes cell apoptosis (Rajagopalan et al., 2002). On the other hand, CUR could induce apoptosis via variable signaling pathways (Karunagaran, Rashmi, & Kumar, 2005). Therefore, DNA fragmentation and apoptosis take place. So, the efficiently delivered MTX/CUR-loaded nanocarrier released its payload intracellularly and acted on the different targets. As a result, enhanced cytotoxicity was observed compared with single-drug-loaded nanocarrier. Also, we compare the cytotoxicity of free MTX/CUR with MTX/CUR-loaded nanocarrier. As depicted in the Figure 7B and 7C, MTX/CUR-loaded nanocarrier indicated a better synergistic effect than free MTX/CUR, since it has significantly smaller  $IC_{50}$ . The increment in the cytotoxicity might be due to the elevated accumulation and efficient release of drugs, which demonstrated the potential of LAFNCC nanocarriers for clinical applications by taking into account their negligible toxicity in MCF-7 and MDA-MB-231 cells, and with high estimation in both kind of normal and cancer cells. Also, according to the studies put forward by Khine et al. about the long-term blood circulation of the cellulose-based nanoplateforms (approximately seven days) (Khine & Stenzel, 2020), the MTX/CUR-LAFNCC NCs can potentially be used for treatment of any types of tumors with active angiogenic phenotype. Notably, in case of superficial tumors they can hold a great promise in localized cancer therapy. Both of the MCF-7 and MDA-MB-231 cells have angiogenic factors.

### 3.6. Morphological assessment of apoptotic cells using DAPI staining

The DAPI staining study was performed to assess the morphological changes induced by apoptosis in MCF-7 and MDA-MB-231 cell lines (Figure 9). In this regard, the chromatin morphology and the density of nuclei were observed after 48 h treatment using fluorescence microscopy. The cells treated with blank nanocarrier revealed no significant morphological changes compared with untreated cells in both cell lines and showed their intact and evenly shapes. In contrast, the images of cells treated with free drugs and dual-drug-loaded formulations showed the sign of apoptosis including, cell shrinkage, loss of cell-cell contact, nuclear fragmentation, and chromatin condensation. In the comparison of these groups, the cells treated with dual drug formulations showed cell shrinkage and chromatin fragmentation intensely in both cell lines. Also, the remaining density of cells treated with different drug formulations is decreased compared to the control cells, suggesting the apoptotic cells engulfing by neighboring cells or professional phagocytes through phagocytosis (B. He, Lu, & Zhou, 2009). Noticeably, MTX/CUR-LAFNCC NCs has a significant effect on both MCF-7 and MDA-MB-231 cell number and morphology changes than MTX-LANCC NCs, CUR-LANCC NCs and free drug formulations, which is consistent with the synergistic effect of MTX and CUR combination in enhancing cytotoxicity.

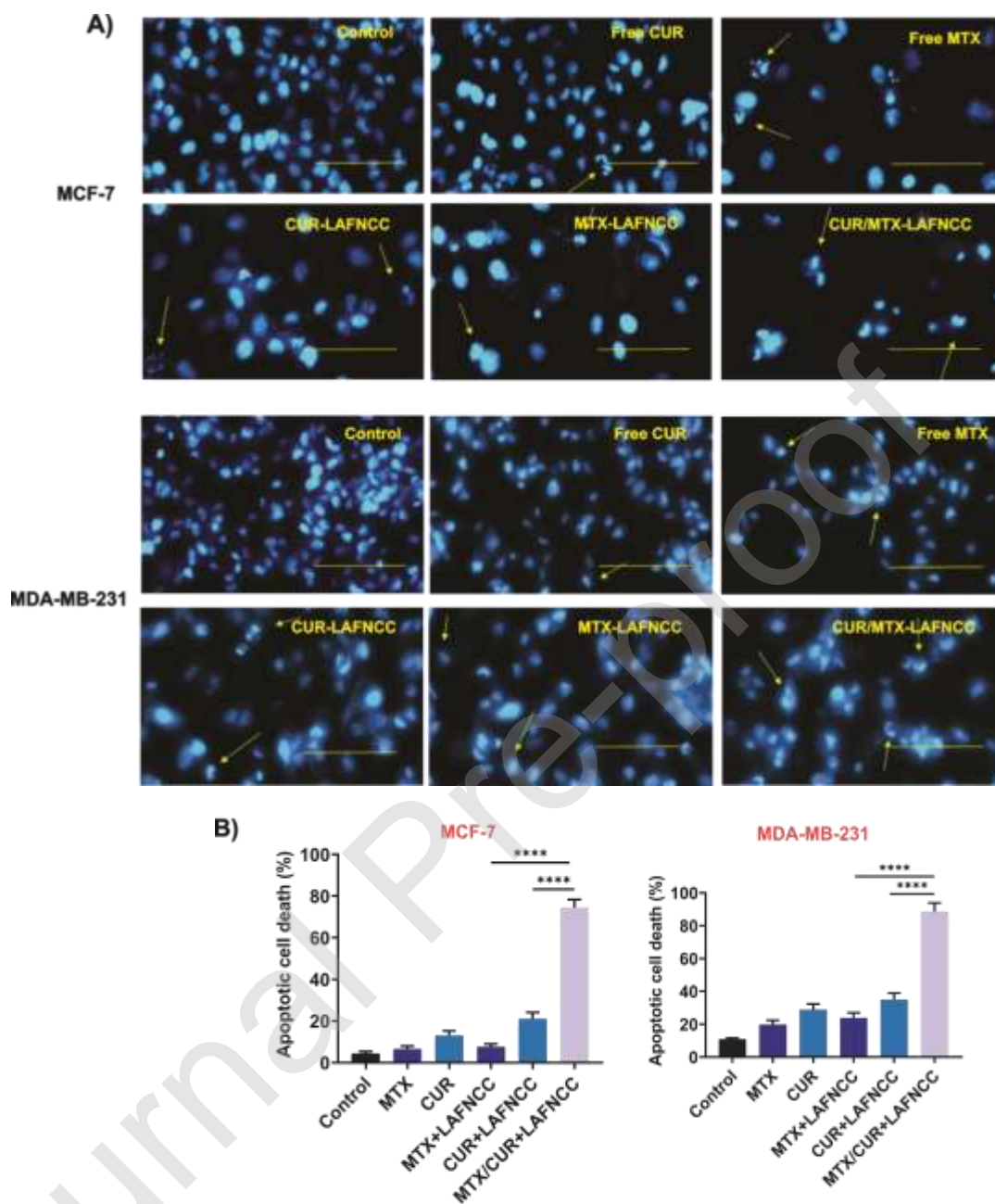


**Figure 9.** Nuclear morphology alteration of MCF-7 and MDA-MB-23 cells. A) Fluorescent images showing the morphology of cells after treated with different MTX and CUR formulations for 48 h. B) The proportion of apoptotic cell death in MCF-7 and MDA-MB-231 treated with single- or dual-drug-loaded NPs. apoptosis was examined by fluorescent microscopy after staining the cells with  $1 \mu\text{g mL}^{-1}$  DAPI solution. To ascertain the proportion of apoptotic cells,  $\geq 100$  stained cells were counted. In both cells, dual-drug-loaded NPs induced highly significantly

apoptosis in comparison to single-drug-loaded NPs. Scale bars represent 100  $\mu\text{m}$ . Images were taken at a magnification 400 $\times$  for both cells.

### 3.7. MTX/CUR induced cell cycle distribution in MCF-7 and MDA-MB-231 cells

Here we evaluate the distribution of cell cycle progression under normal growth conditions (control) and after treatment with different formulations of MTX and CUR as well as blank nanocarrier. The area under the peak was calculated using CellQuest software (Becton Dickinson, San Joes, CA, USA) to determine the phase within the cell cycle. As the results showed, in both cell lines, nanocarrier LAFNCC has no significant effect on cell cycle progression compared with the control cell cycle profile, which further confirmed the biocompatibility of the nanocarrier. The anticancer drug MTX is known to be cell cycle-specific due to the inhibition of DNA synthesis in the S and G2/M phases (Matsushima et al., 1985). As depicted in Figure 10, in the MCF-7 cells treated with free MTX the percentage of cells in the G2/M (0.00%) and S (36.20%) phases decreased while the percentage of cells in G0-G1 increased (63.80%); in contrast, the MDA-MB-231 cells treated with free MTX showed an increase in the percentage of the S phases (34.73%) in comparison to the control cells which emphasized the above mentioned. However, when the cells treated with free CUR, the percentage of cells in the S and G2/M phases increased. Similarly, the treatment of MCF-7 cells with nanoformulated MTX (280  $\mu\text{g}/\text{ml}$ ) and CUR (2  $\mu\text{g}/\text{ml}$ ) for 48 h showed an increased in the percentage of G0-G1 phase for MTX (71.65%), and an increase in the S (56.79%) and G2/M (7.21%) phases for CUR in comparison to control cells (Figure 10A) which is consistent with the previous reports that mentioned CUR as an agent that arrested cell cycle progression in S and G2M phases in human breast cancer cells (Karunagaran et al., 2005). However, when the MDA-MB-231 cells treated with nanoformulated MTX (900  $\mu\text{g}/\text{ml}$ ), CUR (21  $\mu\text{g}/\text{ml}$ ) in the same interval time the percentage of the S phase increased slightly in comparison to control cells (Figure 10B). In the MCF-7 cells, the combined treatment with MTX/CUR-LAFNCC (16  $\mu\text{g}/\text{ml}$ ) indeed increased the percentage of cells in G0-G1 phase (68.98%) and blocked the progression to the S and G2M phases (Figure 12A). Interestingly, the MDA-MB-231 cells treated with MTX/CUR-LAFNCC (43  $\mu\text{g}/\text{ml}$ ) for 48h, showed cell cycle arrest in the G2/M phase (53.12%) with concomitant reduction of cells in G0/G1 (46.88%) and S (0.00%) phases.

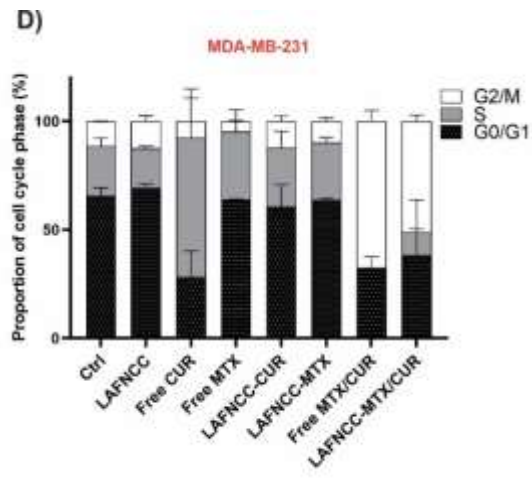
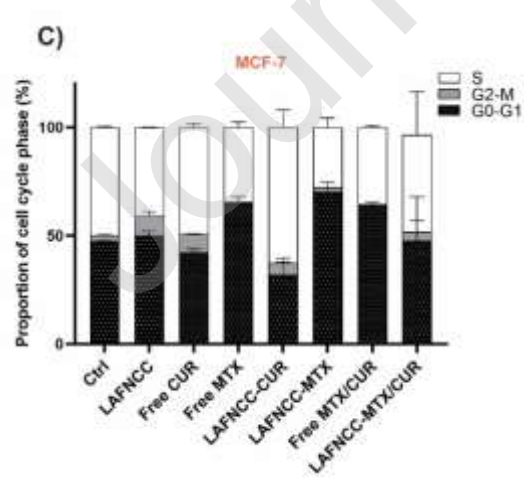
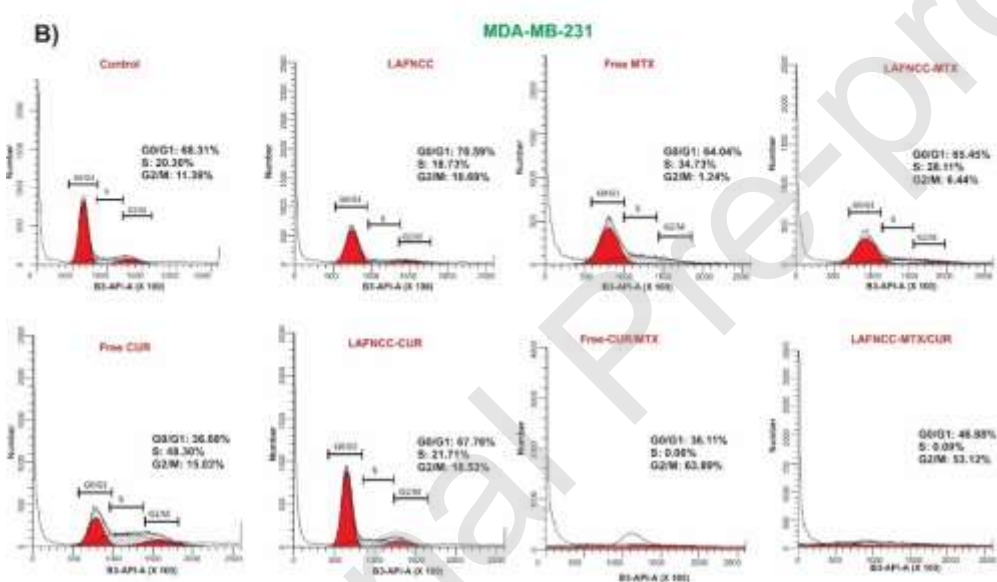
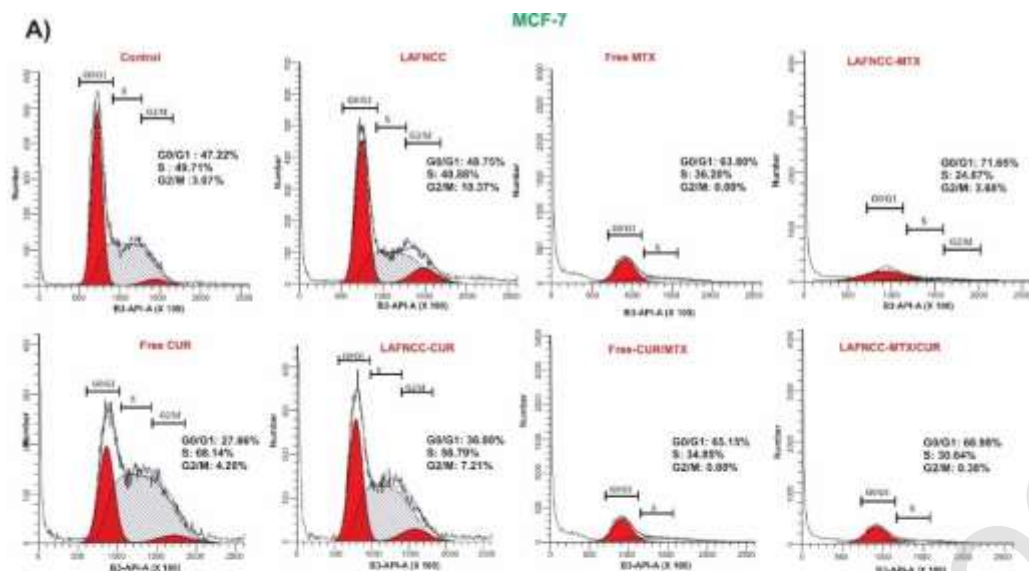


**Figure 10.** Inhibitory effect of different formulations of MTX and CUR on cell cycle progressions of MCF-7 and MDA-MB-231 cells. A-B) Flow cytometry assay of the DNA contents in MCF-7 and MDA-MB-231 cells treated for 48 h with different formulations of MTX and CUR in concentrations around their  $IC_{50}$ . Cell cycle analysis was performed by flow cytometry after staining DNA content with propidium iodide. C-D) DNA distribution percentages in different phases of the cell cycle (G0-G1, S, G2-M) after PI staining in MCF-7 and MDA-MB-231 cells. Data are representative of three independent experiments.

#### 4. Conclusion

In this study, a biocompatible lysine-decorated cellulose-based nanosystem was developed and studied as a potential platform for efficient and sustained delivery of two model drug MTX and CUR in MCF-7 and MDA-MB-231 breast cancer cells. The nanosystem was prepared using mild reaction conditions. The basic platform of the nanocarrier is made up of the cost-effective source cellulose, which is beneficial for clinical application. The resulted nanosystem was characterized in terms of morphology and having the desired modified structure, in which amino acid l-lysine was embedded in amine functionalized nanocrystalline cellulose platform. The fabricated lysine-embedded cellulose nanoparticles with elongate geometry have much longer clearance time compared with the spherical counterparts (Khine & Stenzel, 2020). The high entrapment efficacy and loading content were obtained for MTX and CUR. The *in vitro* release study of the fabricated nanosystem revealed that the model drugs could release in a sustained and acidic-facilitate manner, and by this way it can reduce premature drug release during blood circulation. The results obtained from the cytotoxicity study of the nanosystem demonstrated that CUR as an adjuvant drug synergized the therapeutic efficacy of MTX in the induction of apoptotic cell death for MCF-7 and MDA-MB-231 cancer cells. As a result, dual-drug-loaded NPs could perform more effective than single-drug-loaded NPs or free-drug combinations in killing cancer cells. Moreover, the DAPI staining study and cell cycle analysis further confirmed the successful induction of apoptosis by dual-drug loaded nanocarrier. In conclusion, the lysine-embedded cellulose-based nanosystem could be served as a suitable nanocarrier to achieve efficient multi-drug delivery for combination cancer therapy.

Considering the previous reports about the probable gradual degradation of cellulose in the living body (Khine & Stenzel, 2020; Tao et al., 2018) and taking into account that, our results

confirmed pH-triggered controlled and sustain release of drugs from the nanoplatform which is necessary for blood drug concentration for efficient cancer therapy, the resultant MTX/CUR-LAFNCC nanocarrier has potential for clinical application. Thus, future investigation concerning first about the study of biosafety and biodegradability of the nanocarrier, along with the probable modification of the nanoplatform for clinical application in cancer treatment.

Credit authorship contribution statement:

Sevil Vaghefi Moghaddam: Investigation, Methodology, Project administration, Writing- original draft.

Fatmeh Abedi: Investigation, Methodology.

Effat Alizadeh: Cell culture administration, Writing- review & editing.

Behzad Baradaran: Cell culture administration.

Nasim Annabi: Writing- review & editing.

Abolfazl Akbarzadeh: Supervision, Validation, Writing- review & editing.

Soodabeh Davaran: Validation, Writing- review & editing.

## **Acknowledgment**

This work was supported by the Iran National Science Foundation (INSF) and Deputy of Research and Technology, Ministry of Health and Medical Education, as project NO: 96009006. Also, the Drug Applied Research Center, Tabriz University of Medical Sciences supported this project, as project NO: 58637 (Protection Code of Human Subject in Medical Research: IR.TBZMED.REC.1396.399).

## References

- Abramczyk, H., Surmacki, J., Kopeć, M., Olejnik, A. K., Lubecka-Pietruszewska, K., & Fabianowska-Majewska, K. (2015). The role of lipid droplets and adipocytes in cancer. Raman imaging of cell cultures: MCF10A, MCF7, and MDA-MB-231 compared to adipocytes in cancerous human breast tissue. *Analyst*, *140*(7), 2224-2235.
- Aggarwal, B. B., Kumar, A., & Bharti, A. C. (2003). Anticancer potential of curcumin: preclinical and clinical studies. *Anticancer research*, *23*(1/A), 363-398.
- Ahmed, F., Pakunlu, R. I., Brannan, A., Bates, F., Minko, T., & Discher, D. E. (2006). Biodegradable polymersomes loaded with both paclitaxel and doxorubicin permeate and shrink tumors, inducing apoptosis in proportion to accumulated drug. *Journal of Controlled Release*, *116*(2), 150-158.
- Al-Lazikani, B., Banerji, U., & Workman, P. (2012). Combinatorial drug therapy for cancer in the post-genomic era. *Nat Biotechnol*, *30*(7), 679.
- Aldawsari, H., Raj, B. S., Edrada-Ebel, R., Blatchford, D. R., Tate, R. J., Tetley, L., & Dufès, C. (2011). Enhanced gene expression in tumors after intravenous administration of arginine-, lysine- and leucine-bearing polyethylenimine polyplex. *Nanomedicine: Nanotechnology, Biology and Medicine*, *7*(5), 615-623.
- Araki, J., Wada, M., Kuga, S., & Okano, T. (1998). Flow properties of microcrystalline cellulose suspension prepared by acid treatment of native cellulose. *Colloids and Surfaces A: Physicochemical and Engineering Aspects*, *142*(1), 75-82.
- Azizi Samir, M. A. S., Alloin, F., & Dufresne, A. (2005). Review of recent research into cellulosic whiskers, their properties and their application in nanocomposite field. *Biomacromolecules*, *6*(2), 612-626.
- Bao, Y., He, J., & Li, Y. (2012). Synthesis of novel hyperbranched poly (ester-amide) s based on acidic and basic amino acids via “AD+ CBB” couple-monomer approach. *Polymer*, *53*(1), 145-152.
- Barnes, M. J., Estlin, E. J., Taylor, G. A., Aherne, G. W., Hardcastle, A., McGuire, J., . . . Newell, D. R. (1999). Impact of polyglutamation on sensitivity to raltitrexed and methotrexate in relation to drug-induced inhibition of de novo thymidylate and purine biosynthesis in CCRF-CEM cell lines. *Clinical cancer research*, *5*(9), 2548-2558.
- Beck, S., Bouchard, J., & Berry, R. (2012). Dispersibility in water of dried nanocrystalline cellulose. *Biomacromolecules*, *13*(5), 1486-1494.
- Bessone, F., Argenziano, M., Grillo, G., Ferrara, B., Pizzimenti, S., Barrera, G., . . . Cavalli, R. (2019). Low-dose curcuminoid-loaded in dextran nanobubbles can prevent metastatic spreading in prostate cancer cells. *Nanotechnology*.
- Bitounis, D., Fanciullino, R., Iliadis, A., & Ciccolini, J. (2012). Optimizing druggability through liposomal formulations: new approaches to an old concept. *ISRN pharmaceuticals*, *2012*.
- Boechat, A. L., de Oliveira, C. P., Tarragô, A. M., da Costa, A. G., Malheiro, A., Guterres, S. S., & Pohlmann, A. R. (2015). Methotrexate-loaded lipid-core nanocapsules are highly effective in the control of inflammation in synovial cells and a chronic arthritis model. *International journal of nanomedicine*, *10*, 6603.
- Bray, F., Ferlay, J., Soerjomataram, I., Siegel, R. L., Torre, L. A., & Jemal, A. (2018). Global cancer statistics 2018: GLOBOCAN estimates of incidence and mortality worldwide for 36 cancers in 185 countries. *CA: a cancer journal for clinicians*, *68*(6), 394-424.
- Britcher, L. G., Kehoe, D. C., Matisons, J. G., & Swincer, A. G. (1995). Siloxane coupling agents. *Macromolecules*, *28*(9), 3110-3118.
- Chen, K.-J., Liang, H.-F., Chen, H.-L., Wang, Y., Cheng, P.-Y., Liu, H.-L., . . . Sung, H.-W. (2012). A thermoresponsive bubble-generating liposomal system for triggering localized extracellular drug delivery. *ACS nano*, *7*(1), 438-446.

- Chen, Y.-H., Tsai, C.-Y., Huang, P.-Y., Chang, M.-Y., Cheng, P.-C., Chou, C.-H., . . . Wu, C.-L. (2007). Methotrexate conjugated to gold nanoparticles inhibits tumor growth in a syngeneic lung tumor model. *Molecular pharmaceuticals*, 4(5), 713-722.
- Chieng, B., Lee, S., Ibrahim, N., Then, Y., & Loo, Y. (2017). Isolation and characterization of cellulose nanocrystals from oil palm mesocarp fiber. *Polymers*, 9(8), 355.
- Choi, J., Lee, S. E., Park, J. S., & Kim, S. Y. (2018). Gold nanorod- photosensitizer conjugates with glutathione- sensitive linkages for synergistic cancer photodynamic/photothermal therapy. *Biotechnology and bioengineering*, 115(5), 1340-1354.
- Choi, J. S., Nam, K., Park, J.-y., Kim, J.-B., Lee, J.-K., & Park, J.-s. (2004). Enhanced transfection efficiency of PAMAM dendrimer by surface modification with L-arginine. *Journal of Controlled Release*, 99(3), 445-456.
- Chou, T.-C. (2006). Theoretical basis, experimental design, and computerized simulation of synergism and antagonism in drug combination studies. *Pharmacological reviews*, 58(3), 621-681.
- Chou, T., & Martin, N. (2005). CompuSyn for drug combinations and for general dose-effect analysis, software and user's guide: A computer program for quantitation of synergism and antagonism in drug combinations, and the determination of IC50 and ED50 and LD50 values. *ComboSyn Inc Paramus, NJ*.
- Ciolacu, D., Ciolacu, F., & Popa, V. I. (2011). Amorphous cellulose—structure and characterization. *Cellulose chemistry and technology*, 45(1), 13.
- Cronstein, B. N. (2005). Low-dose methotrexate: a mainstay in the treatment of rheumatoid arthritis. *Pharmacological reviews*, 57(2), 163-172.
- Curcio, M., Mauro, L., Naimo, G. D., Amantea, D., Cirillo, G., Tavano, L., . . . Iemma, F. (2018). Facile synthesis of pH-responsive polymersomes based on lipidized PEG for intracellular co-delivery of curcumin and methotrexate. *Colloids and Surfaces B: Biointerfaces*, 167, 568-576.
- D'Souza, S. (2014). A review of in vitro drug release test methods for nano-sized dosage forms. *Advances in Pharmaceuticals*, 2014.
- Dassanayake, R. S., Gunathilake, C., Dassanayake, A. C., Abidi, N., & Jaroniec, M. (2017). Amidoxime-functionalized nanocrystalline cellulose–mesoporous silica composites for carbon dioxide sorption at ambient and elevated temperatures. *Journal of Materials Chemistry A*, 5(16), 7462-7473.
- Dong, S., Cho, H. J., Lee, Y. W., & Roman, M. (2014). Synthesis and cellular uptake of folic acid-conjugated cellulose nanocrystals for cancer targeting. *Biomacromolecules*, 15(5), 1560-1567.
- Dong, X. M., Revol, J.-F., & Gray, D. G. (1998). Effect of microcrystallite preparation conditions on the formation of colloid crystals of cellulose. *Cellulose*, 5(1), 19-32.
- Doppalapudi, S., Jain, A., Domb, A. J., & Khan, W. (2016). Biodegradable polymers for targeted delivery of anti-cancer drugs. *Expert opinion on drug delivery*, 13(6), 891-909.
- Durmus, Z., Kavas, H., Toprak, M. S., Baykal, A., Altınçekiç, T. G., Aslan, A., . . . Coşgun, S. (2009). L-lysine coated iron oxide nanoparticles: synthesis, structural and conductivity characterization. *Journal of Alloys and Compounds*, 484(1-2), 371-376.
- ElBayoumi, T. A., & Torchilin, V. P. (2009). Tumor-targeted nanomedicines: enhanced antitumor efficacy in vivo of doxorubicin-loaded, long-circulating liposomes modified with cancer-specific monoclonal antibody. *Clinical cancer research*, 15(6), 1973-1980.
- Fitz, D., Jakschitz, T., & Rode, B. M. (2008). The catalytic effect of L-and D-histidine on alanine and lysine peptide formation. *Journal of inorganic biochemistry*, 102(12), 2097-2102.
- Gao, J., Xie, C., Zhang, M., Wei, X., Yan, Z., Ren, Y., . . . Lu, W. (2016). RGD-modified lipid disks as drug carriers for tumor targeted drug delivery. *Nanoscale*, 8(13), 7209-7216.
- Geng, Y., Dalhaimer, P., Cai, S., Tsai, R., Tewari, M., Minko, T., & Discher, D. E. (2007). Shape effects of filaments versus spherical particles in flow and drug delivery. *Nature nanotechnology*, 2(4), 249-255.

- Golshan, M., Salami-Kalajahi, M., Roghani-Mamaqani, H., & Mohammadi, M. (2017). Poly (propylene imine) dendrimer-grafted nanocrystalline cellulose: Doxorubicin loading and release behavior. *Polymer*, *117*, 287-294.
- Greco, F., & Vicent, M. J. (2009). Combination therapy: opportunities and challenges for polymer–drug conjugates as anticancer nanomedicines. *Advanced drug delivery reviews*, *61*(13), 1203-1213.
- Habibi, Y., Lucia, L. A., & Rojas, O. J. (2010). Cellulose nanocrystals: chemistry, self-assembly, and applications. *Chemical Reviews*, *110*(6), 3479-3500.
- Han, L., Tang, C., & Yin, C. (2015). Dual-targeting and pH/redox-responsive multi-layered nanocomplexes for smart co-delivery of doxorubicin and siRNA. *Biomaterials*, *60*, 42-52.
- Han, S. S., Li, Z. Y., Zhu, J. Y., Han, K., Zeng, Z. Y., Hong, W., . . . Zhuo, R. X. (2015). Dual- pH sensitive charge- reversal polypeptide micelles for tumor- triggered targeting uptake and nuclear drug delivery. *Small*, *11*(21), 2543-2554.
- He, B., Lu, N., & Zhou, Z. (2009). Cellular and nuclear degradation during apoptosis. *Current opinion in cell biology*, *21*(6), 900-912.
- He, S., Qi, Y., Kuang, G., Zhou, D., Li, J., Xie, Z., . . . Huang, Y. (2016). Single-stimulus dual-drug sensitive nanoplatforM for enhanced photoactivated therapy. *Biomacromolecules*, *17*(6), 2120-2127.
- Hokkanen, S., Bhatnagar, A., Repo, E., Lou, S., & Sillanpää, M. (2016). Calcium hydroxyapatite microfibrillated cellulose composite as a potential adsorbent for the removal of Cr (VI) from aqueous solution. *Chemical engineering journal*, *283*, 445-452.
- Huang, W., Zhang, J., Dorn, H. C., & Zhang, C. (2013). Assembly of bio-nanoparticles for double controlled drug release. *PLoS one*, *8*(9), e74679.
- Jain, S., Jain, R., Das, M., Agrawal, A. K., Thanki, K., & Kushwah, V. (2014). Combinatorial bio-conjugation of gemcitabine and curcumin enables dual drug delivery with synergistic anticancer efficacy and reduced toxicity. *RSC Advances*, *4*(55), 29193-29201.
- Karunakaran, D., Rashmi, R., & Kumar, T. (2005). Induction of apoptosis by curcumin and its implications for cancer therapy. *Current cancer drug targets*, *5*(2), 117-129.
- Kesharwani, P., & Iyer, A. K. (2015). Recent advances in dendrimer-based nanovectors for tumor-targeted drug and gene delivery. *Drug discovery today*, *20*(5), 536-547.
- Khanjanzadeh, H., Behrooz, R., Bahramifar, N., Gindl-Altmutter, W., Bacher, M., Edler, M., & Griesser, T. (2017). Surface chemical functionalization of cellulose nanocrystals by 3-aminopropyltriethoxysilane. *International journal of biological macromolecules*.
- Khili, F., Borges, J., Almeida, P. L., Boukherroub, R., & Omrani, A. D. (2019). Extraction of cellulose nanocrystals with structure I and II and their applications for reduction of graphene oxide and nanocomposite elaboration. *Waste and Biomass Valorization*, *10*(7), 1913-1927.
- Khine, Y. Y., & Stenzel, M. H. (2020). Surface modified cellulose nanomaterials: a source of non-spherical nanoparticles for drug delivery. *Materials Horizons*.
- Kushwah, V., Katiyar, S. S., Agrawal, A. K., Gupta, R. C., & Jain, S. (2018). Co-delivery of docetaxel and gemcitabine using PEGylated self-assembled stealth nanoparticles for improved breast cancer therapy. *Nanomedicine: Nanotechnology, Biology and Medicine*, *14*(5), 1629-1641.
- Li, N., Zhang, H., Xiao, Y., Huang, Y., Xu, M., You, D., . . . Yu, J. (2019). Fabrication of Cellulose-Nanocrystal-Based Folate Targeted Nanomedicine via Layer-by-Layer Assembly with Lysosomal pH-Controlled Drug Release into the Nucleus. *Biomacromolecules*, *20*(2), 937-948.
- Liu, Y., Fang, J., Kim, Y.-J., Wong, M. K., & Wang, P. (2014). Codelivery of doxorubicin and paclitaxel by cross-linked multilamellar liposome enables synergistic antitumor activity. *Molecular pharmaceuticals*, *11*(5), 1651-1661.
- Liu, Z., Cai, W., He, L., Nakayama, N., Chen, K., Sun, X., . . . Dai, H. (2007). In vivo biodistribution and highly efficient tumour targeting of carbon nanotubes in mice. *Nature nanotechnology*, *2*(1), 47-52.

- Lu, D., Hossain, M. D., Jia, Z., & Monteiro, M. J. (2015). One-pot orthogonal copper-catalyzed synthesis and self-assembly of L-lysine-decorated polymeric dendrimers. *Macromolecules*, *48*(6), 1688-1702.
- Lu, T., Sun, J., Chen, X., Zhang, P., & Jing, X. (2009). Folate- conjugated micelles and their folate-receptor- mediated endocytosis. *Macromolecular bioscience*, *9*(11), 1059-1068.
- Marinescu, G., Patron, L., Culita, D. C., Neagoe, C., Lepadatu, C. I., Balint, I., . . . Cizmas, C. B. (2006). Synthesis of magnetite nanoparticles in the presence of aminoacids. *Journal of Nanoparticle Research*, *8*(6), 1045-1051.
- Martínez-Guerra, J., Palomar-Pardavé, M., Romero-Romo, M., Corona-Avenidaño, S., Rojas-Hernández, A., & Ramírez-Silva, M. (2019). New insights on the Chemical Stability of Curcumin in Aqueous Media at Different pH: Influence of the Experimental Conditions. *Int. J. Electrochem. Sci*, *14*, 5373-5385.
- Martins, T. d. S., Matos, J. d. R., Vicentini, G., & Isolani, P. C. (2005). Synthesis, characterization, spectroscopy and thermal analysis of rare earth picrate complexes with L-lysine. *Journal of thermal analysis and calorimetry*, *82*(1), 77-82.
- Matos Ruiz, M., Cavaille, J., Dufresne, A., Gerard, J., & Graillat, C. (2000). Processing and characterization of new thermoset nanocomposites based on cellulose whiskers. *Composite Interfaces*, *7*(2), 117-131.
- Matsushima, Y., Kanzawa, F., Hoshi, A., Shimizu, E., Nomori, H., Sasaki, Y., & Saijo, N. (1985). Time-schedule dependency of the inhibiting activity of various anticancer drugs in the clonogenic assay. *Cancer chemotherapy and pharmacology*, *14*(2), 104-107.
- Mi, Y., Zhao, J., & Feng, S.-S. (2013). Targeted co-delivery of docetaxel, cisplatin and herceptin by vitamin E TPGS-cisplatin prodrug nanoparticles for multimodality treatment of cancer. *Journal of Controlled Release*, *169*(3), 185-192.
- Mohan Yallapu, M., Ray Dobberpuhl, M., Michele Maher, D., Jaggi, M., & Chand Chauhan, S. (2012). Design of curcumin loaded cellulose nanoparticles for prostate cancer. *Current drug metabolism*, *13*(1), 120-128.
- Molnes, S. N., Paso, K. G., Strand, S., & Syverud, K. (2017). The effects of pH, time and temperature on the stability and viscosity of cellulose nanocrystal (CNC) dispersions: implications for use in enhanced oil recovery. *Cellulose*, *24*(10), 4479-4491.
- Naksuriya, O., Okonogi, S., Schifflers, R. M., & Hennink, W. E. (2014). Curcumin nanoformulations: a review of pharmaceutical properties and preclinical studies and clinical data related to cancer treatment. *Biomaterials*, *35*(10), 3365-3383.
- Park, J. H., von Maltzahn, G., Zhang, L., Derfus, A. M., Simberg, D., Harris, T. J., . . . Sailor, M. J. (2009). Systematic surface engineering of magnetic nanoworms for in vivo tumor targeting. *Small*, *5*(6), 694-700.
- Peer, D., Karp, J. M., Hong, S., Farokhzad, O. C., Margalit, R., & Langer, R. (2007). Nanocarriers as an emerging platform for cancer therapy. *Nature nanotechnology*, *2*(12), 751.
- Persidis, A. (1999). Cancer multidrug resistance. *Nat Biotechnol*, *17*(1), 94-95. doi:10.1038/5289
- Rahimi, M., Safa, K. D., & Salehi, R. (2017). Co-delivery of doxorubicin and methotrexate by dendritic chitosan-g-mPEG as a magnetic nanocarrier for multi-drug delivery in combination chemotherapy. *Polymer Chemistry*, *8*(47), 7333-7350.
- Rahimi, M., Shafiei-Irannejad, V., Safa, K. D., & Salehi, R. (2018). Multi-branched ionic liquid-chitosan as a smart and biocompatible nano-vehicle for combination chemotherapy with stealth and targeted properties. *Carbohydrate polymers*, *196*, 299-312.
- Rajagopalan, P. R., Zhang, Z., McCourt, L., Dwyer, M., Benkovic, S. J., & Hammes, G. G. (2002). Interaction of dihydrofolate reductase with methotrexate: ensemble and single-molecule kinetics. *Proceedings of the National Academy of Sciences*, *99*(21), 13481-13486.
- Rånby, B. G. (1951). Fibrous macromolecular systems. Cellulose and muscle. The colloidal properties of cellulose micelles. *Discussions of the Faraday Society*, *11*, 158-164.

- Revol, J.-F., Godbout, L., Dong, X.-M., Gray, D. G., Chanzy, H., & Maret, G. (1994). Chiral nematic suspensions of cellulose crystallites; phase separation and magnetic field orientation. *Liquid Crystals*, *16*(1), 127-134.
- Roberts, G., Feeney, J., Birdsall, B., Charlton, P., & Young, D. (1980). Methotrexate binding to dihydrofolate reductase. *Nature*, *286*(5770), 309.
- Schneider, C. A., Rasband, W. S., & Eliceiri, K. W. (2012). NIH Image to ImageJ: 25 years of image analysis. *Nature methods*, *9*(7), 671-675.
- Schroeder, A., Honen, R., Turjeman, K., Gabizon, A., Kost, J., & Barenholz, Y. (2009). Ultrasound triggered release of cisplatin from liposomes in murine tumors. *Journal of Controlled Release*, *137*(1), 63-68.
- Segal, L., Creely, J., Martin Jr, A., & Conrad, C. (1959). An empirical method for estimating the degree of crystallinity of native cellulose using the X-ray diffractometer. *Textile research journal*, *29*(10), 786-794.
- Selulosa-Polivinilklorida, S. R. N., SHELAMI, R. M., KARGARZADEH, H., & ABDULLAH, I. (2015). Effects of silane surface treatment of cellulose nanocrystals on the tensile properties of cellulose-polyvinyl chloride nanocomposite. *Sains Malaysiana*, *44*(6), 801-810.
- Singh, V. K., & Subudhi, B. B. (2016). Development and characterization of lysine-methotrexate conjugate for enhanced brain delivery. *Drug delivery*, *23*(7), 2327-2337.
- Song, Y., Zhang, L., Gan, W., Zhou, J., & Zhang, L. (2011). Self-assembled micelles based on hydrophobically modified quaternized cellulose for drug delivery. *Colloids and Surfaces B: Biointerfaces*, *83*(2), 313-320.
- Strimpakos, A. S., & Sharma, R. A. (2008). Curcumin: preventive and therapeutic properties in laboratory studies and clinical trials. *Antioxidants & redox signaling*, *10*(3), 511-546.
- Sunasee, R., Carson, M., Despres, H. W., Pacherille, A., Nunez, K. D., & Ckless, K. (2019). Analysis of the Immune and Antioxidant Response of Cellulose Nanocrystals Grafted with  $\beta$ -Cyclodextrin in Myeloid Cell Lines. *Journal of Nanomaterials*, 2019.
- Tang, H., Guo, J., Sun, Y., Chang, B., Ren, Q., & Yang, W. (2011). Facile synthesis of pH sensitive polymer-coated mesoporous silica nanoparticles and their application in drug delivery. *International journal of pharmaceutics*, *421*(2), 388-396.
- Tao, W., Ji, X., Zhu, X., Li, L., Wang, J., Zhang, Y., . . . Islam, M. A. (2018). Two- dimensional antimonene- based photonic nanomedicine for cancer theranostics. *Advanced Materials*, *30*(38), 1802061.
- Tarvirdipour, S., Vasheghani-Farahani, E., Soleimani, M., & Bardania, H. (2016). Functionalized magnetic dextran-spermine nanocarriers for targeted delivery of doxorubicin to breast cancer cells. *International journal of pharmaceutics*, *501*(1-2), 331-341.
- Tian, Y., Jiang, X., Chen, X., Shao, Z., & Yang, W. (2014). Doxorubicin- loaded magnetic silk fibroin nanoparticles for targeted therapy of multidrug- resistant cancer. *Advanced Materials*, *26*(43), 7393-7398.
- Tie, S.-L., Lin, Y.-Q., Lee, H.-C., Bae, Y.-S., & Lee, C.-H. (2006). Amino acid-coated nano-sized magnetite particles prepared by two-step transformation. *Colloids and Surfaces A: Physicochemical and Engineering Aspects*, *273*(1-3), 75-83.
- Um, Y., Cho, S., Woo, H. B., Kim, Y. K., Kim, H., Ham, J., . . . Lee, S. (2008). Synthesis of curcumin mimics with multidrug resistance reversal activities. *Bioorganic & medicinal chemistry*, *16*(7), 3608-3615.
- Villegas, M., Garcia-Uriostegui, L., Rodríguez, O., Izquierdo-Barba, I., Salinas, A., Toriz, G., . . . Delgado, E. (2017). Lysine-grafted MCM-41 silica as an antibacterial biomaterial. *Bioengineering*, *4*(4), 80.
- Wang, H., Zhao, Y., Wu, Y., Hu, Y.-l., Nan, K., Nie, G., & Chen, H. (2011). Enhanced anti-tumor efficacy by co-delivery of doxorubicin and paclitaxel with amphiphilic methoxy PEG-PLGA copolymer nanoparticles. *Biomaterials*, *32*(32), 8281-8290.

- Wu, S.-Y., Chou, H.-Y., Tsai, H.-C., Anbazhagan, R., Yuh, C.-H., Yang, J. M., & Chang, Y.-H. (2020). Amino acid-modified PAMAM dendritic nanocarriers as effective chemotherapeutic drug vehicles in cancer treatment: a study using zebrafish as a cancer model. *RSC Advances*, *10*(35), 20682-20690.
- Xie, J., Li, Y., Song, L., Pan, Z., Ye, S., & Hou, Z. (2017). Design of a novel curcumin-soybean phosphatidylcholine complex-based targeted drug delivery systems. *Drug delivery*, *24*(1), 707-719.
- Xing, C., Chen, S., Liang, X., Liu, Q., Qu, M., Zou, Q., . . . Fan, D. (2018). Two-dimensional MXene (Ti<sub>3</sub>C<sub>2</sub>)-integrated cellulose hydrogels: toward smart three-dimensional network nanoplatfoms exhibiting light-induced swelling and bimodal photothermal/chemotherapy anticancer activity. *ACS applied materials & interfaces*, *10*(33), 27631-27643.
- Xing, C., Chen, S., Qiu, M., Liang, X., Liu, Q., Zou, Q., . . . Dong, B. (2018). Conceptually novel black phosphorus/cellulose hydrogels as promising photothermal agents for effective cancer therapy. *Advanced healthcare materials*, *7*(7), 1701510.
- Xiong, M.-H., Bao, Y., Yang, X.-Z., Wang, Y.-C., Sun, B., & Wang, J. (2012). Lipase-sensitive polymeric triple-layered nanogel for “on-demand” drug delivery. *Journal of the American Chemical Society*, *134*(9), 4355-4362.
- Xu, H., Yao, Q., Cai, C., Gou, J., Zhang, Y., Zhong, H., & Tang, X. (2015). Amphiphilic poly (amino acid) based micelles applied to drug delivery: The in vitro and in vivo challenges and the corresponding potential strategies. *Journal of Controlled Release*, *199*, 84-97.
- Xu, W., Thapa, R., Liu, D., Nissinen, T., Granroth, S., Närvänen, A., . . . Lehto, V.-P. (2015). Smart porous silicon nanoparticles with polymeric coatings for sequential combination therapy. *Molecular pharmaceutics*, *12*(11), 4038-4047.
- Yin, Y., Tian, X., Jiang, X., Wang, H., & Gao, W. (2016). Modification of cellulose nanocrystal via SI-ATRP of styrene and the mechanism of its reinforcement of polymethylmethacrylate. *Carbohydrate polymers*, *142*, 206-212.
- Yu, J., Ju, Y., Zhao, L., Chu, X., Yang, W., Tian, Y., . . . Dong, Y. (2015). Multistimuli-regulated photochemothermal cancer therapy remotely controlled via Fe<sub>5</sub>C<sub>2</sub> nanoparticles. *ACS nano*, *10*(1), 159-169.
- Zainuddin, N., Ahmad, I., Kargarzadeh, H., & Ramli, S. (2017). Hydrophobic kenaf nanocrystalline cellulose for the binding of curcumin. *Carbohydrate polymers*, *163*, 261-269.
- Zeb, A., Qureshi, O. S., Kim, H.-S., Cha, J.-H., Kim, H.-S., & Kim, J.-K. (2016). Improved skin permeation of methotrexate via nanosized ultradeformable liposomes. *International journal of nanomedicine*, *11*, 3813.
- Zhang, L., Wang, Y., Yang, D., Huang, W., Hao, P., Feng, S., . . . Zan, X. (2019). Shape effect of nanoparticles on tumor penetration in monolayers versus spheroids. *Molecular pharmaceutics*, *16*(7), 2902-2911.
- Zhang, Y., Yang, C., Wang, W., Liu, J., Liu, Q., Huang, F., . . . Kong, D. (2016). Co-delivery of doxorubicin and curcumin by pH-sensitive prodrug nanoparticle for combination therapy of cancer. *Scientific reports*, *6*, 21225.
- Zhao, X., Yang, K., Zhao, R., Ji, T., Wang, X., Yang, X., . . . Hao, J. (2016). Inducing enhanced immunogenic cell death with nanocarrier-based drug delivery systems for pancreatic cancer therapy. *Biomaterials*, *102*, 187-197.
- Zhao, Z., Lou, S., Hu, Y., Zhu, J., & Zhang, C. (2017). A nano-in-nano polymer-dendrimer nanoparticle-based nanosystem for controlled multidrug delivery. *Molecular pharmaceutics*, *14*(8), 2697-2710.
- Zhou, Q.-C., Wu, Z.-H., Chi, S.-Y., & Yang, Q.-H. (2007). Dietary lysine requirement of juvenile cobia (*Rachycentron canadum*). *Aquaculture*, *273*(4), 634-640.